2002

# Use of an Epitaxial BaF2 Buffer Layer on Silicon to Control W03 Thin Film Growth

Luke D. Doucette

# USE OF AN EPITAXIAL $BaF_2$ BUFFER LAYER ON SILICON TO CONTROL $WO_3$ THIN FILM GROWTH

By

Luke D. Doucette

B.S. University of Maine, 2000

A THESIS

Submitted in Partial Fulfillment of the

Requirements for the Degree of

Master of Science

(in Physics)

The Graduate School

The University of Maine

December, 2002

Advisory Committee:

Robert J. Lad, Professor of Physics, Advisor

Charles W. Smith, Professor of Physics

Brian G. Frederick, Assistant Professor of Chemistry

# USE OF AN EPITAXIAL $BaF_2$ BUFFER LAYER ON SILICON TO CONTROL $WO_3$ THIN FILM GROWTH

By Luke D. Doucette

Thesis Advisor: Dr. Robert J. Lad

An Abstract of the Thesis Presented
In Partial Fulfillment of the Requirements for the
Degree of Master of Science
(in Physics)
December, 2002

The electronic and mechanical properties of tungsten trioxide ($WO_3$) thin films have been successfully utilized in both surface acoustic wave and chemiresistive microsensor devices for the detection of certain gas-phase species. A critical material aspect that can affect microsensor performance is the type and degree of crystallization within the sensing film. However, the inclusion of this added dimension into a thin film limits the number of viable substrates for which heteroepitaxy may be realized. For $WO_3$, this constraint has restricted its usage as a sensing material to being primarily coupled with sapphire substrates. Not only does sapphire promote structured film growth in this system, but it also provides the necessary electronic insulation for proper chemiresistive sensor operation.

In this thesis study, we have demonstrated that multi-domained, heteroepitaxial tungsten trioxide films can alternatively be integrated onto silicon (100) oriented substrates by way of a high quality, (111) oriented barium fluoride insulator film buffer layer. Specifically, within an optimal deposition temperature range of 400°C - 500°C,

monoclinic phase $WO_3$ films maintained coexisting (002), (020), and (200) orientations on $BaF_2$(111)/Si(100) substrates. The $WO_3$ films were grown by electron cyclotron resonance oxygen plasma-assisted electron beam evaporation of a $WO_3$ source. A thorough investigation of the $BaF_2$/Si substrate revealed that the $BaF_2$ layer consisted of multiple crystalline domains oriented about the $BaF_2$ [111] axis, which produced similarly oriented domains within subsequent film layers. Further analysis indicated that an interfacial barium tungstate ($BaWO_4$) reaction product formed at the $WO_3$-$BaF_2$ interface. Post-deposition air-anneal experiments indicated that the heteroepitaxial $WO_3$ films maintained their lattice structure when air-annealed for 24 hours at 400°C.

## ACKNOWLEDGEMENTS

This research was funded in part by the Department of Defense (Navy) and the Laboratory for Surface Science and Technology (LASST) at the University of Maine. Additional support came in the form of a Cooperative Research And Development Agreement (CRADA) between LASST and the Naval Surface Warfare Center, Dahlgren Division (NSWCDD). I would like to express my deepest thanks and gratitude to Dr. Robert Lad for providing me this research opportunity, and for the experience and guidance that he shared with me throughout this research effort. I would also like to thank Dr. Charles Smith and Dr. Brian Frederick for serving on my committee and providing constructive criticisms of this work; Dr. George Bernhardt, Dr. William DeSisto, Dr. David Frankel, and Dr. Jay LeGore for their technical assistance during this research endeavor; and to Dr. Francisco Santiago from NSWCDD for providing the substrate material for our research. Finally, the completion of this thesis would not have been possible without the unending patience and support from my wife, Christine, and daughters, Olivia and Gabrielle, to whom I am eternally grateful.

## TABLE OF CONTENTS

## LIST OF TABLES

## LIST OF FIGURES

# CHAPTER 1: INTRODUCTION

## 1.1 Importance of $WO_3$ Thin Films

Tungsten trioxide ($WO_3$) thin films have been used in a wide variety of applications which take advantage of its optical[1-3], tribological[4,5], and electronic features[6-10]. As early as 1973, the optical phenomenon known as electrochromism was first discovered in $WO_3$ by Deb[11]. Electrochromism describes the ability of a material to undergo a reversible color change when an electric field or current is applied[12]. Although electrochromic (EC) properties have since been found in several other transition metal oxide materials (e.g. $MoO_3$, $TiO_2$)[3], $WO_3$ remains one of the most viable material options for EC devices to date. In addition, $WO_3$ has generated interest in tribological applications as a solid lubricant for high-temperature, oxidizing environments. Specifically, $WO_3$ coatings have been reported to maintain low friction and low wear at temperatures up to 800°C.[4]

Over the past decade, the electronic and mechanical behavior of $WO_3$ thin films have been studied at the University of Maine in regards to its application for surface acoustic wave (SAW)[8,10] and semi-conducting metal oxide (SMO) chemiresistive[6,7,9] gas sensing devices. A SAW device functions on the principle that, due to gas interactions, the mechanical properties of the metal oxide film become altered so as to produce a change in the velocity and/or attenuation of a surface acoustic wave propagating through the sensing material. In chemiresistive devices, the primary gas sensing mechanisms arise from reduction/oxidation surface reactions occurring between the film and a gas phase species. Provided that the metal oxide film is fully oxidized through the film formation process or upon suitable annealing in an oxygen environment, such interactions between

film and gas can induce a reversible change of the films resistivity via promotion of electrons into the conduction band by either oxygen loss/vacancies or insertion of electropositive gas atoms within the film.[13] In particular, chemiresistive sensing devices that utilize these electronic properties of $WO_3$ films have reported sensitivities as low as 10 parts per million (ppm) for $NO_2$ and $NH_3$ gases exposures, and 1 part per billion (ppb) when exposed to test gases such as $H_2S$.[7] These results have motivated continuing research on $WO_3$ thin films for microsensor applications.

## 1.2 Heteroepitaxial $WO_3$ Films for Microsensor Applications

One of the key material parameters that can affect sensor performance is the crystallographic orientation of the film relative to the substrate, or epitaxy. Recent work on $WO_3$ SMO sensing films has demonstrated this fact. Conductivity and gas exposure studies indicate that epitaxially oriented films produce larger conductivity and gas responses as compared to polycrystalline films.[14,15] In addition, typical operating temperatures for chemiresistive sensors (100°C to 500°C) can lead to thermally induced changes within the sensing film microstucture. Such changes produce variable sensor response and/or drift in baseline conductivity for long-term measurements. The presence of a well-defined microstructure can offer increased stability in sensor performance versus unstructured, or amorphous, film structures. Finally, structured films provide suitable platforms for the subsequent deposition of catalytic particles (e.g. Pd, Pt, Au) to induce selectivity towards specific target gases. Therefore, with regards to $WO_3$ sensing films, an increased fundamental understanding of sensor response characteristics and

optimization of sensor performance becomes directly linked with our knowledge and ability to control the production of crystalline $WO_3$ thin films.

Synthesis of well-defined film microstructures generally requires a contaminant-free environment to ensure the purity of the film during formation, which can be readily accomplished with a variety of ultra high vacuum (~$10^{-10}$ torr) deposition systems. Specifically, $WO_3$ thin films have been synthesized by molecular beam expitaxy (MBE) methods such as DC/RF magnetron sputtering, e-beam and thermal evaporation, as well as chemical vapor deposition (CVD), sol-gel, and anodization.[1-11] The clean environment coupled with the ability to limit growth rates to as low as approximately 5 – 6 Å/min. allows control over the fabrication process at an atomic level.

In addition to the deposition method, the ability to realize epitaxy for a deposited film can also strongly depend upon a suitable choice of substrate material. Specifically, for epitaxial film growth, it is generally desired to minimize the interfacial lattice misfit between the substrate and film. Generally, there are two types of film epitaxy which are distinguished as 1) homoepitaxy (i.e. film and substrate are the same material) and 2) heteroepitaxy (i.e. film and substrate are different materials). The differences between these two types of epitaxy are illustrated in Figure 1.1.[16] In homoepitaxy, since the epilayer and substrate crystal structures are perfectly matched, no interfacial strain exists between the film and substrate. For heteroepitaxy, the interfacial lattice parameters are unmatched, where the degree of mismatch can be classified in one of three possible states. If the mismatch is very small (~1% or less), then the situation is essentially that of homoepitaxy. However, if the lattice parameters between substrate and film substantially differ, then film epitaxy may be accommodated by strain or relaxation effects occurring

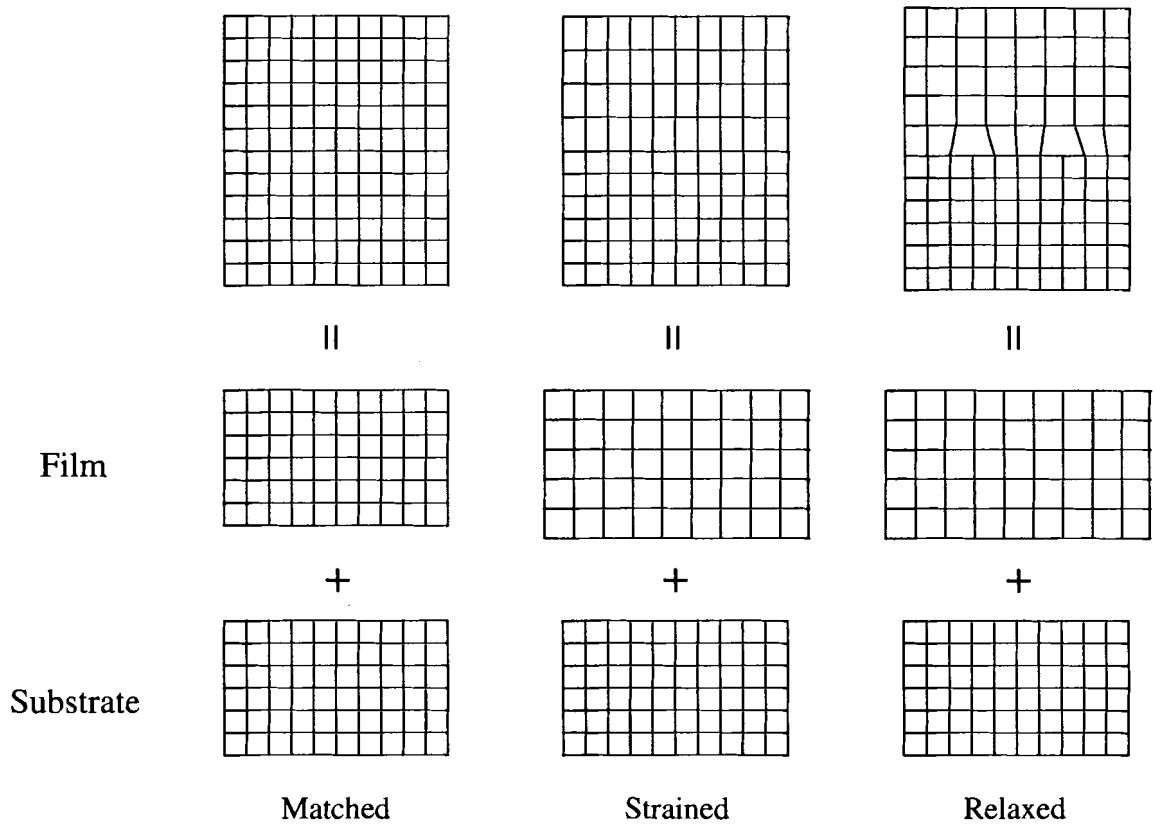


Figure 1.1: Schematic illustration of lattice-matched, strained, and relaxed heteroepitaxial structures. Homoepitaxy is structurally very similar to lattice-matched heteroepitaxy. (from Reference 16)

at the interface. Strained epitaxy typically occurs between film-substrate pairs that possess the same crystal structure, but different lattice constants. As such, the two lattices strain to adjust for this discrepancy. Relaxed epitaxy arises from edge dislocation defects that form at the interface, and generally predominates during the later stages of film formation irrespective of crystal structure or lattice parameter differences.

When lattice mismatch, or misfit, becomes too large, mediation of the film structure by the substrate surface mesh is significantly compromised, often resulting in random polycrystalline or amorphous film structures. To provide an upper limit on this misfit while still realizing epitaxy, a basic theory that accounts for strain/relaxation at the interface was introduced by Frank and van der Merwe[16] that addresses this concern. The

theory predicts that a film layer having a lattice mismatch of less than ~ 9% with the substrate lattice will grow pseudomorphically. This entails an elastic straining in the initial film layers such that atoms on either side of the interface coherently line up. As the film thickness increases, new layers eventually decompose into a relaxed growth structure via dislocations so as to reduce the total elastic strain energy associated with the initial seed layers. What results is a relaxed epitaxial film consisting of an array of misfit dislocations separated by wide regions of relatively good fit.

### 1.3 Current Limitations of $WO_3$ Microsensor Technology

The successful growth of heteroepitaxial $WO_3$ thin films has been limited to a small number of viable substrates, which include MgO[17], $SrTiO_3$[18], and $\alpha$-$Al_2O_3$[19] (i.e. sapphire) single crystals wafers. For gas sensors, sapphire is typically used since it is a good electrical insulator, thereby allowing accurate measurement of conductivity changes to be the result of gas-film interactions only. In addition, the relatively small in-plane lattice misfits between certain cuts of sapphire and various crystal phases of $WO_3$ promotes heteroepitaxial film growth on these substrates, satisfying another desired material property of the sensing layer.

One of the main challenges for sapphire-based SMO microsensors has been their integration with existing silicon-based microelectronic packaging technologies. A desirable option for expanding SMO sensor technology would then be to integrate such a sensing film directly onto a silicon platform. Although some metal-oxide films exhibiting heteroepitaxy have been successfully deposited onto silicon substrates[20,21], this appears to be more the exception than the rule. The disparity in lattice constants between

Si (~ 5.4 Å) and most metal oxides (~ 6 – 8 Å) simply introduces too large a misfit at the film-substrate interface for subsequent film epitaxy to evolve. Another major problem is silicide alloy formation at SMO/Si interfaces, which can alter the desired chemical makeup of the sensing film. In terms of sensor operation, provided a crystalline $WO_3$ film could be integrated onto a silicon substrate, the issue of electronically isolating the film for proper sensor functioning still remains due to the semiconducting nature of most conventional silicon substrates.

### 1.4 Research Motivation

Our research focused on demonstrating the feasibility of integrating a heteroepitaxial $WO_3$ film onto a Si substrate by way of a highly crystalline, cubic structured barium fluoride ($BaF_2$) thin film buffer layer for microsensor applications. The lattice constant of cubic $BaF_2$ is approximately 6.2 Å, where highly crystalline $BaF_2$ thin films on Si substrates have been obtained.[22,23] In addition, $BaF_2$ has also been well documented to possess excellent insulating qualities for semiconductor on insulator (SOI)[24] and metal/insulator/semiconductor (MIS)[25] electronic device applications. Both of these physical attributes of $BaF_2$ satisfy the aforementioned limitations of direct integration, therefore providing an appropriate bridge between silicon and SMO thin films for microsensor technology.

### 1.5 Thesis Objectives and Overview

The primary objective of this investigation was to establish the optimum deposition parameters via MBE technology for the heteroepitaxial growth of $WO_3$ films on

$BaF_2$(111)/Si(100) substrates. We employed electron cyclotron resonance (ECR) oxygen plasma assisted e-beam evaporation of $WO_3$ pellets as the particular deposition technique. Post-deposition film characterization involved X-ray photoelectron spectroscopy (XPS) for chemical analysis; reflection high-energy electron diffraction (RHEED) and x-ray diffraction (XRD) for crystal structure/orientation analysis. In addition, to better understand the resultant microstructure(s) within the $WO_3$ films, considerable analysis of the $BaF_2$ surface mesh was performed. Specifically, low energy electron diffraction (LEED) for surface structure, atomic force microscopy (AFM) for surface morphology and roughness, as well as XPS, RHEED, and XRD were employed to fully analyze the $BaF_2$ substrate layer. Since chemiresistive SMO microsensors typically operate between 100°C and 400°C to activate specific reactions and hasten diffusion kinetics, post-deposition air-anneal studies were performed in order to examine the stability of the $WO_3$ microstructure under these typical sensor operating conditions. The annealing experiments also served to further our understanding of the material interactions at the $WO_3$-$BaF_2$ interface, where a barium tungstate ($BaWO_4$) reaction product layer was observed to form. To that end, an interfacial reaction and growth model is proposed to explain the evolution of the entire $WO_3$/$BaWO_4$ composite system.

In this thesis, a brief review of the $BaF_2$ and $WO_3$ bulk crystal systems is given. In addition, a theoretical review of the primary characterization methods and an overview of the experimental facilities/procedures are provided. Finally, characterization results, analysis and conclusions of our research are presented.

## 1.6 Collaborative Efforts

This investigation has been performed within the general guidelines of a Cooperative Research And Development Agreement (CRADA) between the Laboratory for Surface Science and Technology (LASST), University of Maine, and the Naval Surface Warfare Center, Dahlgren Division (NSWCDD), Dahlgren, Virginia. As part of this agreement, a collaboration was established to synthesize SMO chemiresistive thin films (e.g. $WO_3$) at LASST, and fabricate $BaF_2$/Si substrates at NSWCDD.

## 1.7 Chapter References


[1] K Miyake, H. Kaneko, M. Sano, N. Suedomi, "Physical and electrochromic properties of the amorphous and crystalline tungsten oxide thick films prepared under reducing atmosphere", *J. Appl. Phys.* 55 (1984) 2747-2753.

[2] A. Agrawal, H. Habibi, "Effect of heat treatment on the structure, composition and electrochromic properties of evaporated tungsten oxide film", *Thin Solid Films* 169 (1989) 257-270.

[3] K. Marszalek, "Magnetron-sputtered $WO_3$ films for electrochromic devices" *Thin Solid Films* 175 (1989) 227-233.

[4] S.F. Murray, S.J. Calabrese, "Effects of solid lubricants on low speed sliding behavior of silicon nitride at termperstures to 800°C", *Lubr. Eng.* 49 (1993) 387.

[5] O.D. Greenwood, S.C. Moulzolf, P.J. Blau, R.J. Lad, "The influence of microstructure on tribological properties of $WO_3$ thin films", *Wear* 232 (1999) 84-90.

[6] E.P.S. Barrett, G.C. Georgiades, P.A. Sermon, "The mechanics of operation of $WO_3$-based $H_2S$ Sensors", *Sens. Actuators B* 1 (1990) 116-120.

[7] D.J. Smith, J.F. Vetelino, R.S. Falconer, E.L. Wittman, "Stability, sensitivity, and selectivity of tungsten trioxide films for sensing applications", *Sen. Actuators B* 13-14 (1993) 264-268.

[8] L.J. LeGore, K. Snow, J.D. Galipeau, J.F. Vetelino, "The optimization of a tungsten trioxide film for application in a surface acoustic wave gas sensor", *Sens. Actuators B* 35-36 (1996) 164-169.

[9] M. Penza, C. Martucci, G. Cassano, "$NO_x$ gas sensing characteristics of $WO_3$ thin films activated by noble metals (Pd, Pt, Au) layers", *Sens. Actuators B* 50 (1998) 52-59.

[10] M. Penza, L Vasanelli, "SAW $NO_x$ gas sensor using $WO_3$ thin-film sensitive coating", *Sens. Actuators B* 41 (1997) 31-36.

[11] S. Deb, "Optical and photoelectric properties and colour centres in thin films of tungsten oxide" *Philos. Mag.* 27 (1973) 801-822.

[12] E. Lassner and W. Schubert, Tungsten: Properties, Chemistry, Technology of the Element, Alloys, and Chemical Compounds, New York: Kluwer Academic / Plenum Publishers (1999).

[13] C.N.R. Rao, B. Raveau, Transition Metal Oxides, New York:VCH Publishers (1995).

[14] H.T. Sun, C. Cantalini, L. Lozzi, M. Passacantando, S. Santucci, M. Pelino, "Microstructural effect on $NO_2$ sensitivity of $WO_3$ thin film gas sensors Part 1. Thin film devices, sensors and actuators", *Thin Solid Films* 287 (1996) 258-263.

[15] M.D. Antonik, J. E. Schneider, E. L. Wittman, K. Snow, J.F. Vetelino, R.J. Lad, "Microstructural effects in $WO_3$ gas-sensing films", *Thin Solid Films* 256 (1995) 247-252.

[16] M. Ohring, The Materials Science of Thin Films, 2nd ed.,London: Academic Press (2002).

[17] Y. Kobayashi, S. Terada, K. Kubota, "Epitaxial growth of $WO_3$ thin films on MgO and $Al_2O_3$", *Thin Solid Films* 168 (1989) 133-139.

[18] A. Garg, J.A. Leake, Z.H. Barber, "Epitaxial growth of $WO_3$ films on $SrTiO_3$ and sapphire", *J. Phys. D* 33 (2000) 1048-1053.

[19] L.J. LeGore, O.D. Greenwood, J.W. Paulus, D.J. Frankel, R.J. Lad, "Controlled growth of $WO_3$ films", *J. Vac. Sci. Technol. A* 15 (1997) 1223-1227.

[20] M. Yoshimoto et al., "Room-temperature epitaxial growth of $CeO_2$ thin films on Si(111) substrates for fabrication of sharp oxide/silicon interface", *Jpn. J. Appl. Phys. Part 2: Letters* 34 (1995) L688-L690.

[21] V.E. Drozd, A.P. Baraban, I.O. Nikiforava, V.B. Aleskoviski, "Synthesis and investigation of heterooxides by ML-ALE method", *Appl. Surf. Sci.* 12 (1997) 264-268.

[22] M.F. Stumborg, F. Santiago, T.K. Chu, K.A. Boulais, "Deposition of GaAs (111) epilayers on $BaF_2$ (111)Si (100) heterostructures by molecular beam epitaxy", *J. Vac. Sci. Techol. A* 15 (1997) 2473-2477.

[23] T.K. Chu, F. Santiago, M. Stumborg, C.A. Huber, "The role of barium in the heteroepitaxial growth of insulator and semiconductors on silicon", *Mat. Res. Soc. Symp. Proc.* 334 (1994) 501-506.

[24] H.C. Lu, H.R. Fetterman, C.J. chen, C. Hsu, T. M. Chen, "Growth and characterization of MBE-grown thin films of InSb on Si", *Solid-State Electron.* 36 (1993) 533-538.

[25] Ito, Akihiro; Tsuji, Kiyoshige; Hosomi, Takeshi; Maki, Tetsuro; Kobayashi, Takeshi, "Improved stability of metal-insulator-diamond semiconductor interface by employing $CaF_2$/thin $BaF_2$ composite insulator film", *Jpn. J. Appl. Phys.* 39 (2000) 4755-4756.

# CHAPTER 2: CRYSTALLOGRAPHIC PROPERTIES OF THE SUBSTRATE AND FILM SYSTEMS

## 2.1 Bulk Crystal Structure of the $BaF_2$ Substrate

The bulk crystal lattice structure of $BaF_2$ is that of the *fluorite* structure with space group *F*m3m, which is an overall face centered cubic (fcc) conventional cell arrangement, illustrated in Figure 2.1 below.[1] The conventional cubic-cell is shown in Figure 2.1 as the black wire frame, with barium atoms located at the cube corners. Specifically, the system is comprised of a fcc Ba sub-lattice and a simple cubic F sub-lattice situated at the (¼ ¼ ¼) positions of the conventional cell / Ba sub-lattice. Published values for the *a* lattice constant of bulk $BaF_2$, which is the side length of the conventional cell, render a spacing of 6.20 Å.[1,2] As such, each barium atom resides at the

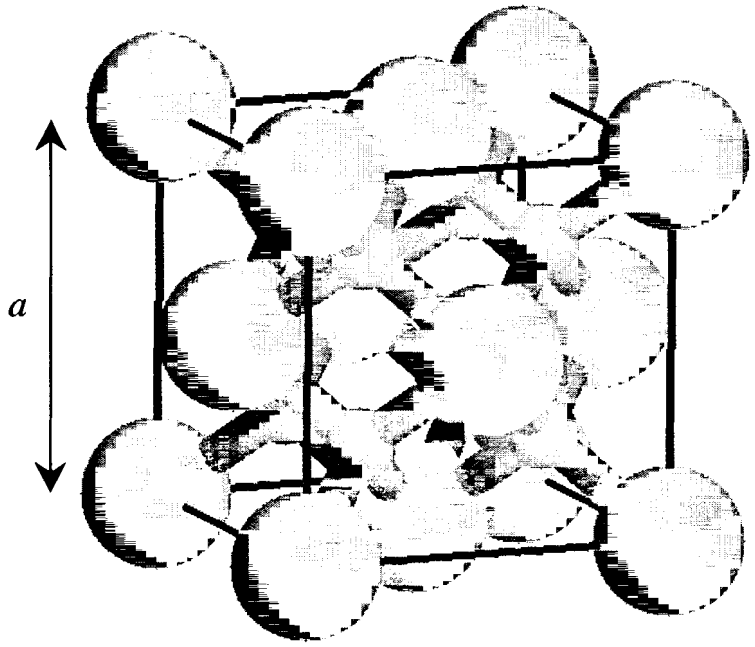


Figure 2.1: $BaF_2$ conventional cell crystal structure. Barium and fluorine atoms are shown as large/light gray and small/dark gray spheres, respectively.

center of eight fluorine atoms situated at the corners of a cubic sub-structure. In turn, each fluorine atom is therefore in a tetrahedral coordination with barium atoms.

To better understand the nature of the $BaF_2$ (111) growth surface, an electron counting method, or autocompensation principle,[3] can be employed to predict whether the bulk structure is barium or fluoride terminated. Originally applied to explain semiconductor surface reconstructions and since extended to predict the surface structures of insulators, the autocompensation principle is based on the assumption that the most likely surface structure is the one that greatly reduces the surface energy. Specifically, this can be accomplished by the pairing up of anion and cation dangling bonds that are produced when a particular bulk termination of the material is made. The surface energy is then minimized by the specific surface termination (i.e. anion, cation or reconstruction thereof) that fully occupies the anion dangling bonds and completely empties the cation dangling bonds. The bonds between anion and cation atoms are assumed to be covalent with two electrons per bond, where the barium and fluorine atoms contribute two and seven valence electrons when bonding, respectively. Therefore, the tetrahedral coordinated fluorine anions donate $\frac{7}{4}$ electrons per bond (i.e. 7 valence electrons divided by 4 bonds), whereas the eight-fold coordinated barium cations donate ¼ electrons per bond (i.e. 2 valence electrons divided by 8 bonds).

A (111) $BaF_2$ surface consists of either Ba or F bulk terminations, which are illustrated in Figures 2.2a and 2.2b, respectively. For the Ba bulk truncation, the (111) surface is not autocompensated since the Ba surface atoms each contain four dangling bonds, whereas the last layer of F atoms are fully occupied (Figure 2.2c). However, for the F bulk truncation, we see that this surface is autocompensated since the one dangling F

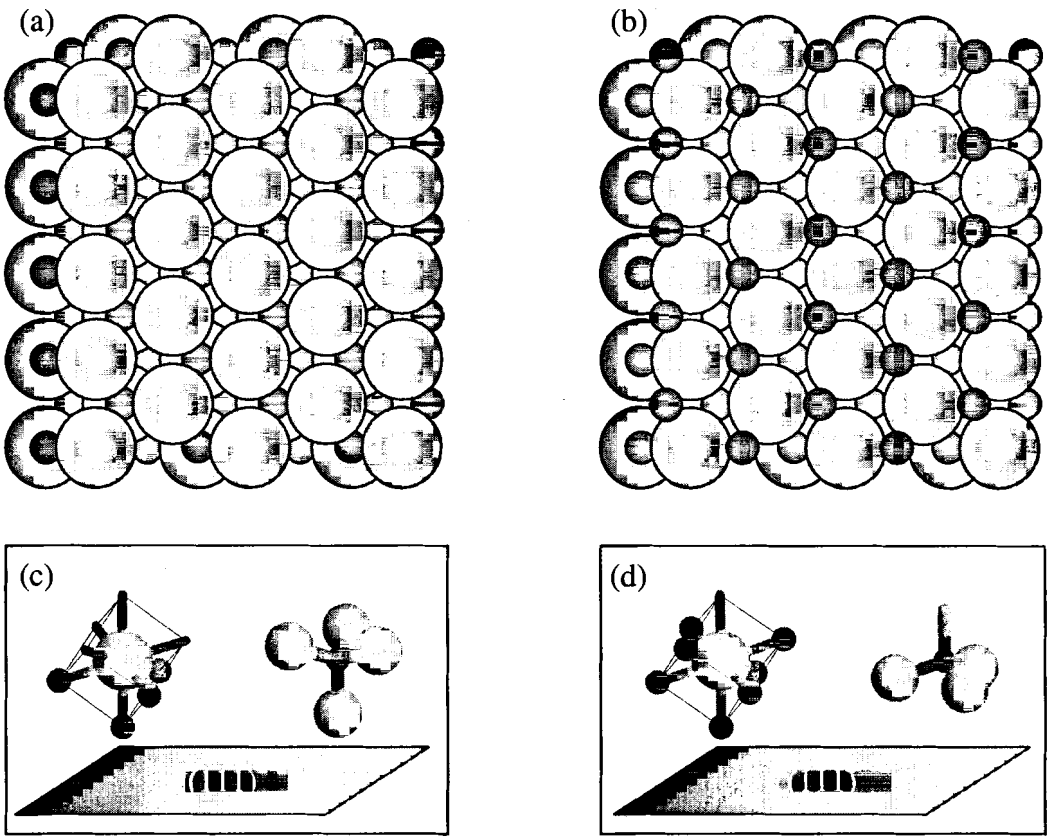


Figure 2.2 – Hard spheres models of the bulk truncated $BaF_2$ (111) surface showing the (a) barium terminated and (b) fluorine terminated surfaces. The specific bond occupancies for the top layers of barium and fluorine atoms are shown for the (c) barium terminated and (d) fluorine terminated (111) surface. Barium and fluorine atoms are large/light gray and small/dark gray spheres, respectively.

bond produced by this termination can be filled by charge transfer from the one dangling Ba bond (Figure 2.2d) the next layer down. Therefore, based on the minimization of the surface energy via the autocompenstation principle, the surface structure for $BaF_2$ (111) is likely F terminated.

## 2.2 Bulk Crystal Structure of $WO_3$

In general, the tungsten-oxygen system is very complex since several stable binary (e.g. $WO_3$, $WO_{2.9}$, $W_{2.72}$,$WO_2$) and tungstate (e.g. $BaWO_4$) structures exist.[4] When fully

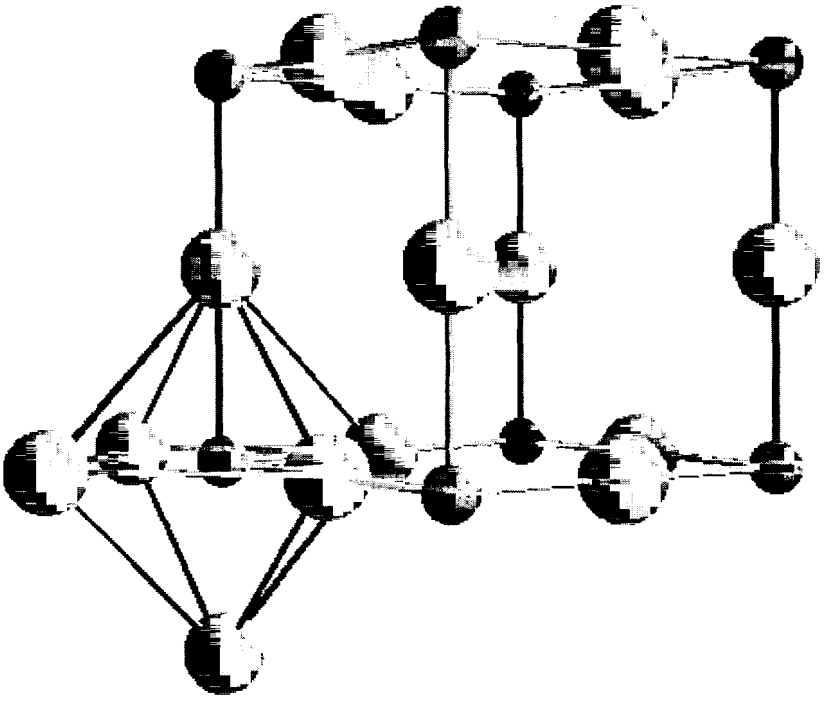

Figure 2.3 - $ReO_3$ type structure showing the octahedral arrangement about the metal atom. Metal (i.e. tungsten) and oxygen atoms are small/dark and large/light spheres, respectively.

oxidized ($W^{6+}$), the atomic arrangement of crystalline $WO_3$ is a distortion of the rhenium oxide cubic lattice; the idealized $ReO_3$ cubic structure is shown in Figure 2.3.[4,5] Within this arrangement, each hexavalent tungsten atom is situated at the center of an octahedron of six oxygen atoms. Numerous variations of this structure for the $WO_3$ system arise due to the relatively smaller tungsten atoms becoming displaced from the centers of the corner sharing octahedra. These displacements result in an overall tilting and/or rotation of the octahedra with respect to one another in order to accommodate for the repositioned tungsten atoms. The extent of these distortions from the ideal cubic form is primarily temperature dependent. The principal allotropic structures of bulk equilibrium $WO_3$ are outlined in Table 2.1.

Table 2.1 - Principal bulk equilibrium phases of $WO_3$ (from References 4,6)

| Phase / S.G. | *a* (Å) | *b* (Å) | *c* (Å) | α | β | γ | Stability Range |
|---|---|---|---|---|---|---|---|
| Triclinic/ P1 | 7.30 | 7.52 | 7.69 | 88.8 | 90.9 | 90.9 | (-50) - 17 °C |
| Monoclinic / $P2_1/n$ | 7.30 | 7.54 | 7.69 | 90 | 90.9 | 90 | 17 - 330 °C |
| Orthorhombic / Pmnb | 7.34 | 7.55 | 7.73 | 90 | 90 | 90 | 330 - 740 °C |
| Tetragonal / P4/nmm | 5.27 | - | 3.92 | 90 | 90 | 90 | above 740 °C |

## 2.3 Chapter References


[1] R.W.G. Wyckoff, Crystal Structures, Vol. 1, New York: Wiley (1964).

[2] JCPDS International Centre for diffraction Data (1997).

[3] J. P. LaFemina, "Theory of insulator surface structures", Handbook of Surface Science, Vol. 1, Ed. W. N. Unertl, New York: Elesevier (1996) 137-184.

[4] E. Lassner and W. Schubert, Tungsten: Properties, Chemistry, Technology of the Element, Alloys, and Chemical Compounds, New York: Kluwer Academic / Plenum Publishers (1999).

[5] C.N.R. Rao, B. Raveau, Transition Metal Oxides, New York: VCH Publishers (1995).

[6] L.J. LeGore, O.D. Greenwood, J.W. Paulus, D.J. Frankel, R.J. Lad, "Controlled growth of $WO_3$ films", *J. Vac. Sci. Technol. A* 15 (1997) 1223-1227.

# CHAPTER 3: THEORETICAL BACKGROUND FOR THIN FILM CHARACTERIZATION METHODS

This chapter explains some of the fundamental concepts underlying the primary characterization methods utilized in this investigation. The intent is to establish the theoretical bases from which conclusions shall be drawn in later chapters. In-depth discussions concerning the more subtle aspects of the following material can be found in the chapter references.

## 3.1 X-Ray Photoelectron Spectroscopy

Chemical surface analysis of materials by XPS is accomplished by irradiating a given specimen with mono-energetic soft X-rays and measuring the kinetic energy of the ejected electrons. In particular, electrons from the surface region are ejected by the photoelectric effect, and possess energies in accord with the following relationship:

$$KE = h\nu - BE - \phi_s \qquad (3-1)$$

where $h\nu$ is the incident photon energy, $BE$ is the binding energy of the electron, and $\phi_s$ is the work function which depends on both the specimen and spectrometer.[1] For most XPS applications, Mg Kα (1253.6 eV) or Al Kα (1486.6 eV) X-rays are utilized since both maintain narrow line widths (0.7 and 0.85 eV, respectively), corresponding to increased resolution, as well as large probe energies that enable core level analysis. Once ejected, a certain cross-section of photoelectrons enters an energy analyzer (e.g. Hemi-Spherical Capacitance Analyzer (HSCA)), which discriminates the kinetic energy of the photoelectrons. For capacitance-type analyzers, information regarding numbers of ejected electrons vs. binding energy is obtained by linearly varying in time the voltage

across the capacitor plates. Since each element has a unique set of core level binding energies, elemental identification and chemical state analysis can be performed by appropriately identifying major photoelectron peaks against the known binding energies.

The surface sensitivity of XPS is primarily due to the small inelastic mean free path ($\lambda$) of the photoelectrons generated within the analyzed specimen. Specifically, for kinetic energies ranging from 10 - 1000 eV, values for $\lambda$ are typically on the order of 2 – 10 atomic layers for most materials according to the universal curve established by Seah and Dench.[1] In general, 95% of the detected photoelectron signal originates from a surface region limited to a vertical depth $d$ defined by

$$d = 3\lambda\sin\alpha \qquad (3-2)$$

where $\alpha$ is the take-off angle of the electrons relative to the surface. Within this surface depth region, photoelectrons that experience no energy losses (i.e. elastically scattered) produce binding energy peaks indicative of the elemental composition of the surface. The photoelectrons that experience inelastic energy losses due to multiple scattering events contribute to the spectrum background. Assuming a take-off angle normal to the surface, the chemical information contained within an XPS spectrum pertains to surface material residing at approximately 6 to 30 atomic layers (~ 20 to 100 Å) within the analyzed specimen.

Quantitative information may also be obtained from XPS spectral scans by measuring relative elemental concentrations, which in turn can reveal the chemical stoichiometry of the surface. In particular, for a homogeneous sample, the number of photoelectrons per second ($I$) in a spectrum (which corresponds to the area under a particular photoelectron peak) is given by the following expression:

$$I = (n)(S) \qquad (3-3)$$

where $n$ corresponds to the number of atoms per $cm^3$, and $S$ is an atomic sensitivity factor which accounts for the physical parameters of the specimen and transmission characteristics of the analyzer (which includes $\lambda$, X-ray flux, photoelectric cross-section for the atomic orbital of interest, sample area, angular efficiency factor, efficiency in the photoelectric process, and detection efficiency).[2] Tables for atomic sensitivity factors are available for specific analyzer geometries, and are expressed relative to other elements, such as Ag. This approach leads to a general expression for the atomic fraction, $C_x$, of any constituent within the specimen:

$$C_x = \frac{n_x}{\sum_i n_i} = \frac{\frac{I_x}{S_x}}{\sum_i \frac{I_i}{S_i}} \qquad (3-4)$$

The indiscriminate application of sensitivity factors can possibly lead to significant errors in this calculation due to the uniqueness of the transmission characteristics from one energy analyzer to the next. Therefore, greater accuracy may be achieved by developing 'in house' sensitivity factors via measurement of a known standard, and/or stoichiometric corroboration via structural analysis.

### 3.2 Kinematic Diffraction Theory and Bragg's Law

For a determination of crystal lattice spacings and symmetries, single-scattering (or kinematic) diffraction theory is sufficient. Kinematic diffraction assumes elastic scattering processes only, and does not account for the multiple scattering events that a scattered particle (e.g. electron, photon) may experience. As such, from single-scattering theory, it is well known that the amplitude of a scattered wave can be expressed as:[3,4]

$$A = \left\{ \sum_l \exp(-i\vec{K} \bullet \vec{r}_l) \right\} \times \left\{ \sum_p f_p \exp(-i\vec{K} \bullet \vec{r}_p) \right\} \qquad (3-5)$$

$$= \{\text{sum over lattice points}\} \times \{\text{sum over atoms in basis}\}$$

where the intensity $I(\vec{K})$ of the scattered wave is equal to $A^2$. The first bracketed term, called the lattice structure factor, sums over all of the lattice points positioned at $\vec{r}_l$ within the crystal structure, and consequently dictates the direction for which diffraction occurs. The second term is a sum over the basis of atoms within the unit cell, where $\vec{r}_p$ is the position of the atom relative to the lattice point defined at the unit cell origin. This second term is called the geometrical structure factor, and it determines the relative intensities of the diffracted beams. Concentrating on the lattice structure factor, $\vec{K}$ and $\vec{r}_l$ are defined as follows:

$$\vec{K} = \vec{k}' - \vec{k} \quad \text{where} |\vec{k}'| = |\vec{k}| = \frac{2\pi}{\lambda} \qquad (3-6)$$

$$\vec{r}_l = u\vec{a} + v\vec{b} + w\vec{c} \quad u,v,w \equiv \text{integers} \qquad (3-7)$$

In these expressions, $\vec{a}, \vec{b}, \text{and } \vec{c}$ are the real space lattice vectors that define the crystal lattice structure; $\vec{K}$, called the scattering vector, is the difference between the diffracted and incident wave vectors, $\vec{k}'$ and $\vec{k}$, respectively, which are equal in magnitude for elastic scattering. The summation in the first term can be broken into a product of three summations, separating out the $\vec{a}, \vec{b}, \text{and } \vec{c}$ vectors via the definition for $\vec{r}_l$. A large scattering amplitude is thus obtained when the individual terms in the sum achieve unity. This obviously occurs when:

$$\vec{K} \bullet \vec{a} = 2\pi h, \ \vec{K} \bullet \vec{b} = 2\pi k, \ \vec{K} \bullet \vec{c} = 2\pi l \quad h,k,l \equiv \text{integers} \qquad (3-8)$$

which are known as the Laue conditions for diffraction from a 3-D lattice. It can be shown that the values of the scattering vector $\vec{K}$ which satisfy the Laue conditions lie on what is called the reciprocal lattice, which is defined as follows:[3,4]

$$\vec{G}_{hkl} = h\vec{a}^* + k\vec{b}^* + l\vec{c}^* \qquad (3-9)$$

where

$$\vec{a}^* = \frac{2\pi(\vec{b}\times\vec{c})}{\vec{a}\bullet(\vec{b}\times\vec{c})},\ \vec{b}^* = \frac{2\pi(\vec{c}\times\vec{a})}{\vec{a}\bullet(\vec{b}\times\vec{c})},\ \vec{c}^* = \frac{2\pi(\vec{a}\times\vec{b})}{\vec{a}\bullet(\vec{b}\times\vec{c})} \qquad (3-10)$$

Therefore, when the scattering vector $\vec{K} = \vec{G}_{hkl}$, the Laue equations are satisfied and diffraction occurs. Furthermore, it can be shown by simple geometry that:[3,4]

$$|\vec{G}_{hkl}| = \frac{2\pi}{d_{hkl}} \qquad (3-11)$$

where $d_{hkl}$ is the interplanar distance for the $(hkl)$ plane in the Miller indices notation.

The diffraction effects dictated by the periodicity of the crystal lattice are also modulated by the value of the structure factor. The simplest situation occurs when the lattice unit cell basis consists of one atom, which can be defined to coincide with the origin of the unit cell coordinate system. The structure factor would then contain only one term in the sum, for which $\vec{r}_p = 0$. As such, from equation (3-5), the only variation in the diffracted beams intensity would depend on $f_p$, called the atomic form factor, which is generally a smoothly varying function. However, for a non-trivial unit cell basis, evaluation of the structure factor can produce cancellations in diffracted beams, resulting in the so-called 'forbidden' reflections. When the resulting intensity function is summed over the entire crystal lattice containing $N_1 \times N_2 \times N_3$ unit cells, we arrive at what is known as the interference function for the scattered particles:[4]

$$I(\vec{K}) = f_p^2 \left\{ \frac{\sin^2\left(\frac{N_1\vec{K}\bullet\vec{a}}{2}\right)}{\sin^2\left(\frac{\vec{K}\bullet\vec{a}}{2}\right)} \right\} \times \left\{ \frac{\sin^2\left(\frac{N_2\vec{K}\bullet\vec{b}}{2}\right)}{\sin^2\left(\frac{\vec{K}\bullet\vec{b}}{2}\right)} \right\} \times \left\{ \frac{\sin^2\left(\frac{N_3\vec{K}\bullet\vec{c}}{2}\right)}{\sin^2\left(\frac{\vec{K}\bullet\vec{c}}{2}\right)} \right\} \qquad (3-12)$$

Inspection of equation (3-12) reveals that the angular spread of the produced diffracted beams will decrease by $(N_{1,2,3})^{-1}$ as $N_1$, $N_2$, and $N_3$ increase, eventually approaching the general form of a 3-D delta function in the limit as $N_1$, $N_2$, and $N_3$ approach infinity

A simple but useful relationship that is entirely consistent with precepts of kinematic diffraction was first developed by Bragg, and follows from the geometry given in Figure 3.1. Specifically, when a wave (e.g. em-radiation or electron) is incident upon a crystal lattice at some angle θ, there arises certain discrete directions for the incident ray that produce strong 'reflections' due constructive interference with other reflected waves. In particular, if the incident waves are monochromatic, having wavelength λ, then reflections from subsequent planes of atoms separated a distance *d* apart will interfere constructively provided the phase difference for the reflected waves is $n\lambda$, where *n* is a

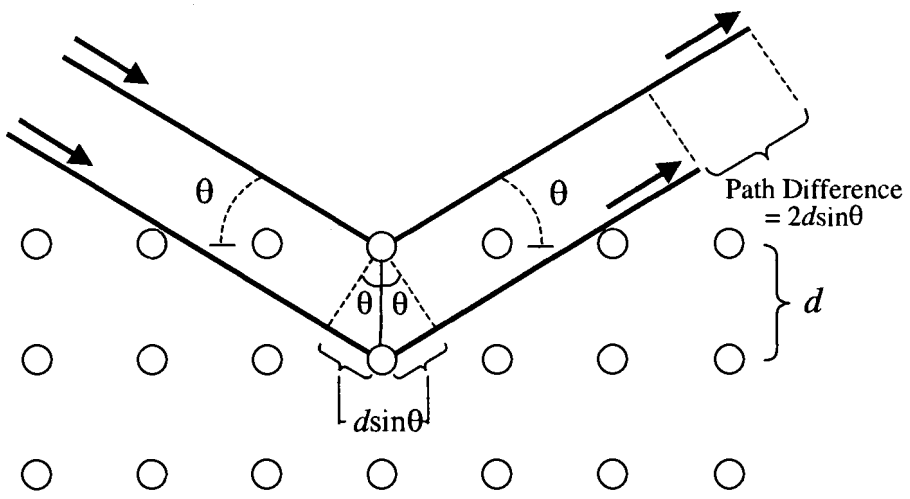


Figure 3.1: Bragg diffraction

positive integer. From this reasoning, we can arrive at the following condition for constructive interference known as Bragg's law:

$$2d\sin\theta = n\lambda \qquad (3-13)$$

Although Bragg's law correctly predicts the basic diffraction phenomenon, it fails to explain many other diffraction events. For instance, it does not provide information as to diffracted beam intensity. In addition, the assumption that $\theta_{incident} = \theta_{reflected}$ implies that diffraction effects only arise due to specular reflection of the incident wave. In fact, the incident waves are scattered spherically in all directions, and therefore a more rigorous scattering theory is required to accurately describe the ensuing diffraction effects.

Despite these simplifications of actual scattering processes, Bragg's law provides a good working definition for diffraction, and in practice (e.g. XRD) is commonly utilized due to its simplicity. To see that Bragg's law is consistent with scattering theory, we consider a vector scattering interpretation of the Bragg case as illustrated in Figure 3.2. In this form, it can be seen that $\vec{K}$ is perpendicular to the lattice plane (recall $|\vec{k}'| = |\vec{k}|$ for elastic scattering), and consequently parallel to $\vec{G}_{hkl}$. By equating $|\vec{K}| = |\vec{G}_{hkl}|$, the

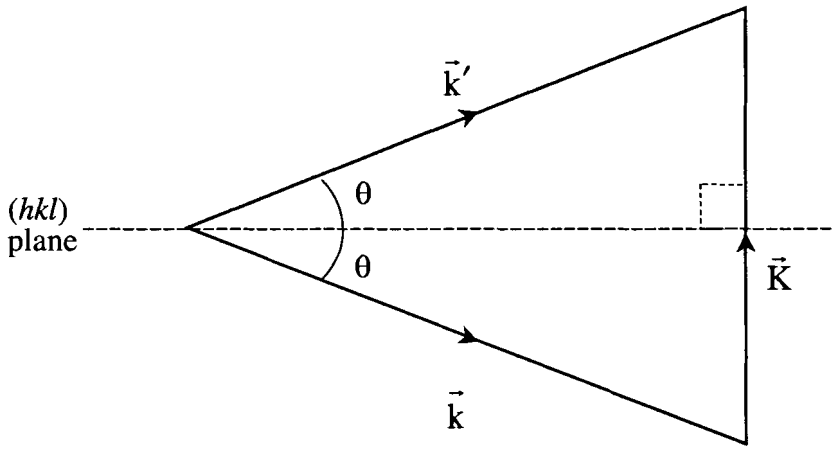


Figure 3.2: Vector diagram of the scattering vector, $\vec{K}$.

Laue conditions for diffraction are thus satisfied:

$$|\vec{K}| = 2|\vec{k}|\sin\theta = \frac{4\pi}{\lambda}\sin\theta = |\vec{G}_{hkl}| = \frac{2\pi}{d_{hkl}}$$

$$\text{or } 2d_{hkl}\sin\theta = \lambda \qquad (3-14)$$

However, this gives us Bragg's law for first order diffraction. Therefore, Bragg's law is completely consistent with the Laue formulation for diffraction.

### 3.3 Applications of Kinematic Diffraction Theory

The following sub-sections describe three specific material characterization techniques (RHEED, LEED, and XRD) that were utilized for determining both the substrate and thin film crystallography within this investigation. Although more complete explanations for each method would require dynamical (or multiple scattering) diffraction theory, the kinematic simplifications of section 3.2 are sufficient for the data interpretation described in this thesis.

#### 3.3.1 Reflection High Energy Electron Diffraction (RHEED)

RHEED is a powerful surface science technique for structural characterization of thin film growth. During this process (Figure 3.3), an incident electron beam strikes a sample surface at a grazing angle $\theta$ of approximately 1-3°, where electron energies typically range from 10 keV to as high as 1000 keV.[5] The diffraction of incident electrons from the sample surface is then projected onto a RHEED detector (e.g. phosphor coated screen), where the resulting diffraction pattern is associated with the reciprocal lattice of the surface structure. Figure 3.5(a) shows typical RHEED pattern generated from a single crystal, r-cut sapphire surface (i.e. $\alpha$-$Al_2O_3$ $(10\bullet\bar{2})$. By calibrating the

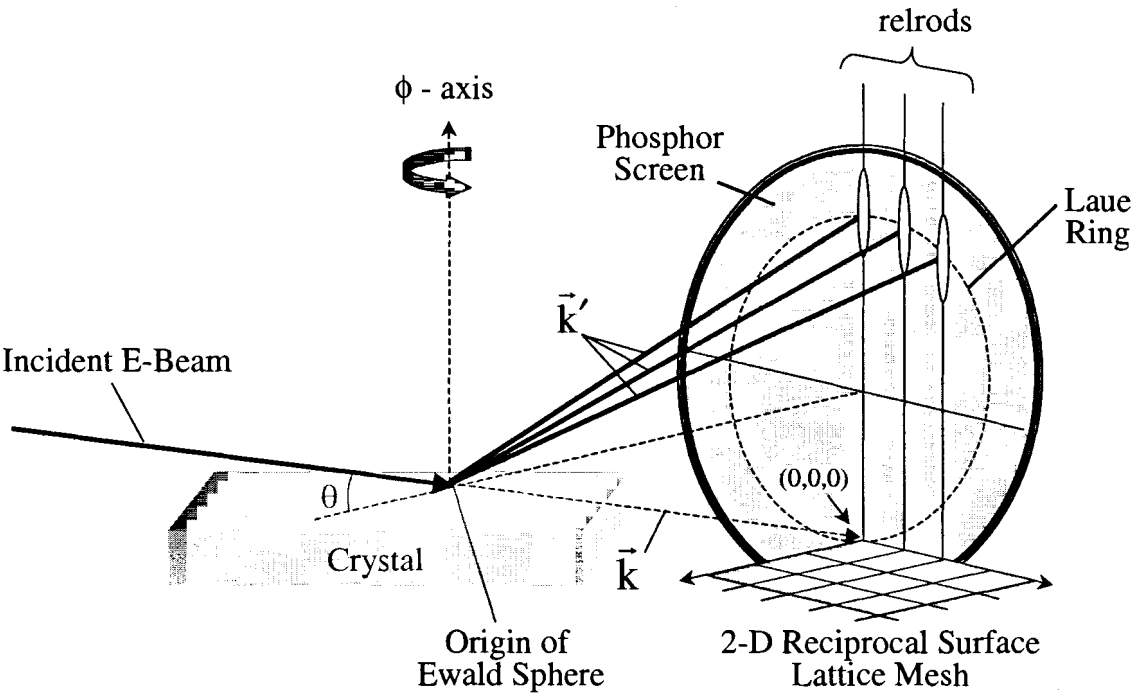


Figure 3.3: Schematic of RHEED from a bulk crystal surface. The Laue ring defines a cross-section through the Ewald sphere.

RHEED/detector system with a known standard, crystallographic information about unknown materials or deposited films can then be determined. In particular, by rotating the sample in the azimuthal ($\phi$) direction, crystal symmetries and lattice spacings can be obtained by using the diffraction transformation equations (3-9) through (3-11), which relate real and reciprocal lattice space vectors.

To better understand the geometry of a typical RHEED pattern, we consider the Ewald sphere construction, which is consistent with the kinematic approximations for diffraction.[5-7] Specifically, the Ewald sphere is an imaginary sphere in momentum space having a radius of magnitude $|\vec{k}|$ (i.e. the incident electron wave vector). A property of this construction is that the only possible directions for diffracted beams occur at the intersections of the sphere with the reciprocal lattice mesh of the crystal. Figure 3.3

shows one such intersection, defined as a Laue ring. Due to the shallow angle of incidence in RHEED, electron diffraction primarily occurs from the 2-D surface mesh of the crystal specimen. As such, the contribution to a diffracted beam intensity due to the sample thickness is negligible (e.g. $N_3 << N_1$ and $N_2$), causing broadening of the beam intensity in the direction normal to the sample surface in accord with equation (3 – 12).

The intensity associated with each reciprocal lattice site overlaps with neighboring sites in the normal direction, producing a continuous streak of intensity. In terms of measurement, this intensity overlap effectively modifies the 3-D reciprocal lattice into an array of reciprocal lattice rods, or "relrods", emanating from, and normal to, the 2-D reciprocal lattice associated with the surface mesh of the sample (see Figure 3.3). Conversely, the relrods posses a finite width due to the larger number of coherent scatterers that are included within the 2-D surface mesh (e.g. $N_1$ and $N_2$), where lattice imperfections and thermal vibrations may give rise, in some cases, to major deviations in this width. Furthermore, the Ewald sphere is also of finite thickness due to the energy spread of the incident electrons. Therefore, the intersection of sphere and relrods occurs over some distance along their height, thereby producing vertical streaks rather than distinct diffraction spots. This 'smearing out' of the intersection may also lead to the inclusion of multiple Laue Zones (i.e. different planes of relrods parallel to the projection screen) within a single diffraction pattern.

During MBE film growth, "transmission diffraction" often occurs due to electron beam penetration of 3-D crystallite island and/or surface asperity growth formations.[8-10] Since the diffraction medium is no longer restricted to an idealized 2-D surface, but now occurs through a true 3-D crystal/crystallite, beam broadening in the surface normal

direction is significantly reduced such that no intensity overlap occurs (e.g. $N_3$ comparable to $N_1$ and $N_2$). As in the 2-D case, diffraction events coincide with the intersection of the Ewald sphere and reciprocal lattice, where again this interaction occurs over some distance along a Laue Zone(s). However, unlike the case for reflection, the transmission diffraction pattern is now composed of distinct spots as opposed to vertical streaks. These spots correspond to the intersection of the sphere with specific reciprocal lattice sites as opposed to relrods.

### 3.3.2 Low Energy Electron Diffraction (LEED)

In the LEED process, an incident low energy electron beam (e.g. 10 – 1000 eV) is directed normal to the sample surface, and the resulting elastically backscattered electrons are once again governed by kinematic diffraction processes.[7,11] As shown in Figure 3.4, the backsattered electrons are intercepted by a system of grids, or wire

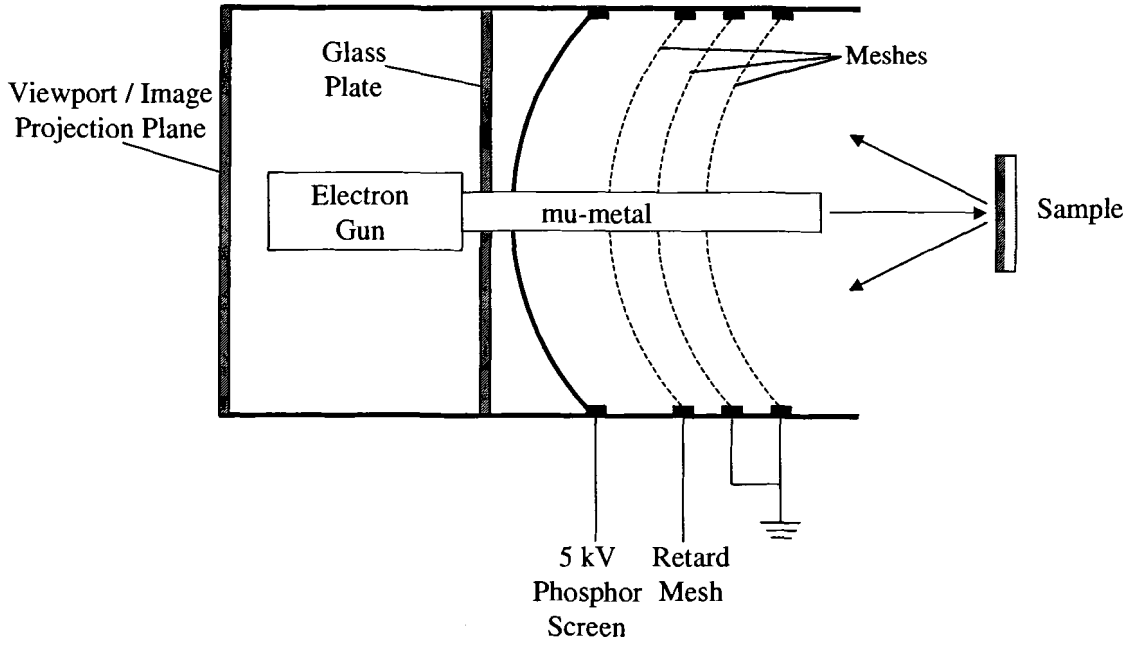


Figure 3.4: Schematic of a 3-mesh LEED optics assembly.

meshes, maintained at different electric potentials. In general, systems of two, three and four mesh versions of the rear view LEED optics systems are available. For the three mesh system depicted in Figure 3.4, the first two meshes encountered are maintained at ground so as to provide a field free region. The phosphor detection screen is then held at a potential of approximately 5 kV, while the mesh nearest the screen (i.e. retard mesh) is at a negative potential close in value to the accelerating energy of the electron gun. The retard mesh therefore has the effect of preventing inelastically scattered electrons from reaching the screen. However, the diffracted (elastic) electrons of higher energy pass through, and are further accelerated by a high potential to illuminate the hemispherical phosphor screen. Figure 3.5(b) shows typical LEED pattern of a single crystal r-cut sapphire sample.

As with RHEED, the LEED pattern is a diffraction pattern that is associated with the 2-D reciprocal lattice of the sample surface mesh. This is due to the low beam penetration distance (usually the top few monolayers) at typical incident electron

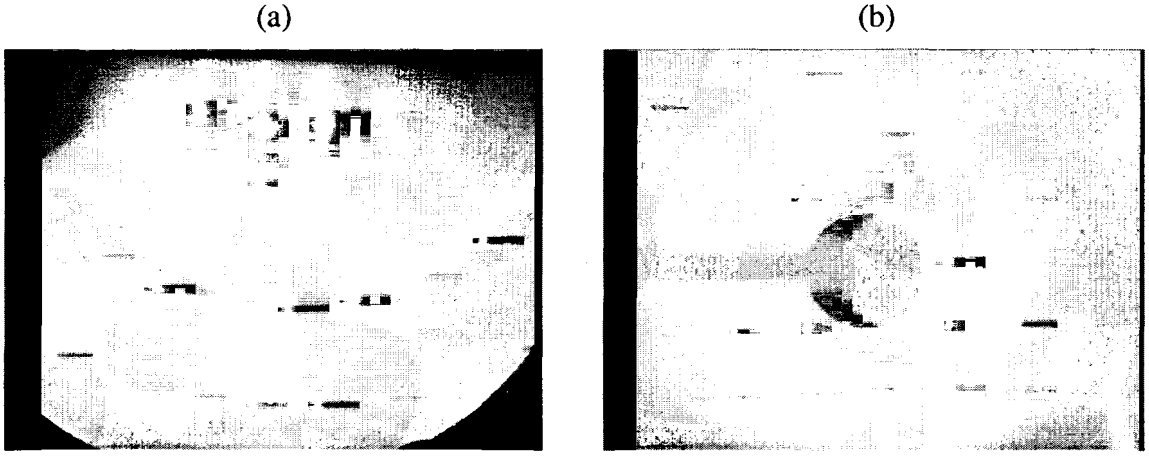


Figure 3.5 (a) 30 keV RHEED pattern of r-cut sapphire. Multiple Laue Zones are visible, as indicated by the semi-circular spot patterns. (b) 100 eV LEED pattern of r-cut sapphire. The shadow is due to the position of the electron gun. Both patterns were obtained with the characterization facilities at LASST.

energies. As before with RHEED, diffraction events occur at the intersection of the relrods and Ewald sphere. However, due to the lower electron energies in the LEED configuration, the Ewald sphere is much smaller than that for RHEED. This increased curvature is accounted for by the hemispherical shape of the detection screen. The projected diffraction pattern image plane is also parallel to the sample plane as opposed to being perpendicular as in RHEED. The result is a sharper diffraction pattern since the intersection of the relrods with the Ewald sphere is more direct from this vantage point. Furthermore, in comparison to RHEED, the interpretation of LEED patterns is usually more straightforward since a single projected pattern represents a single reciprocal plane of the analyzed surface.

### 3.3.3 X-Ray Diffraction (XRD)

Depending upon the specimen and type of radiation used, a number of X-ray crystallography methods can be experimentally employed. The most common techniques are the Laue, Debye-Scherrer (or powder diffraction), or three- and four-circle diffractometer methods.[12] For single crystal structure analysis, the four-circle diffractometer with point detector arrangement is preferred. The relationship between the coordinate axes of a four-circle diffractometer is shown in Figure 3.6. The mechanical assembly that comprises the sample holder, X-ray source, detector and associated gearing is referred to as the goniometer. Within the four-circle arrangement, several standard scan types have been developed that utilize the degrees of freedom provided by the goniometer axes. Specifically, in the Bragg-Brentano geometry, reflections are detected in accord with Bragg's law only from crystallographic planes whose normal vector

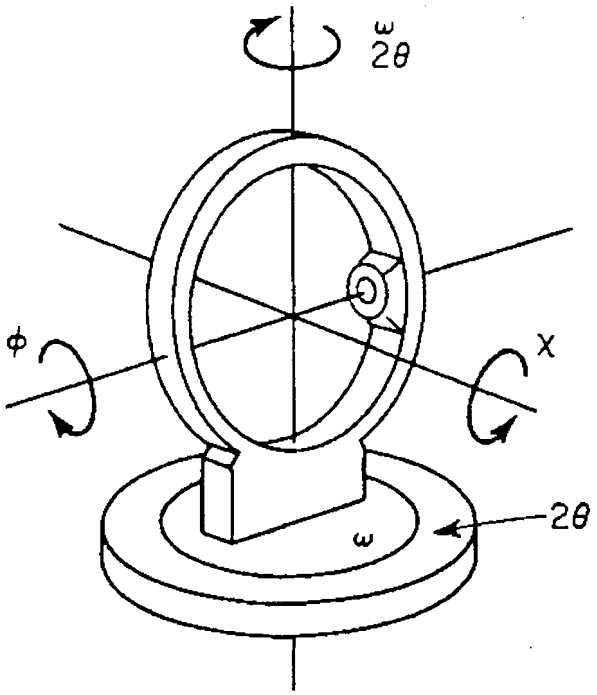


Figure 3.6: Four-circle XRD axes.

bisects the angle between the source and detector. This can be accomplished in one of two ways: with a fixed source, having the sample and detector simultaneously rotate through θ and 2θ, respectively (i.e. θ-2θ scan); and with the sample stationary, having the source and detector simultaneously rotate through equal but opposite θ (i.e θ-θ scan). In practice, for flat samples placed upon a flat sample holder, the Bragg condition for diffraction can only by satisfied by the set of crystallographic planes parallel to the sample surface.

To allow for the complete analysis of textured, polycrystalline, and/or preferred crystalline orientations within a flat specimen, it becomes necessary to detect crystallographic planes that are not aligned parallel to the specimen surface. Such information is obtainable by way of pole figures; Figure 3.7 shows the pole figure geometry first introduced by Schulz.[13] Satisfaction of the Bragg condition is then

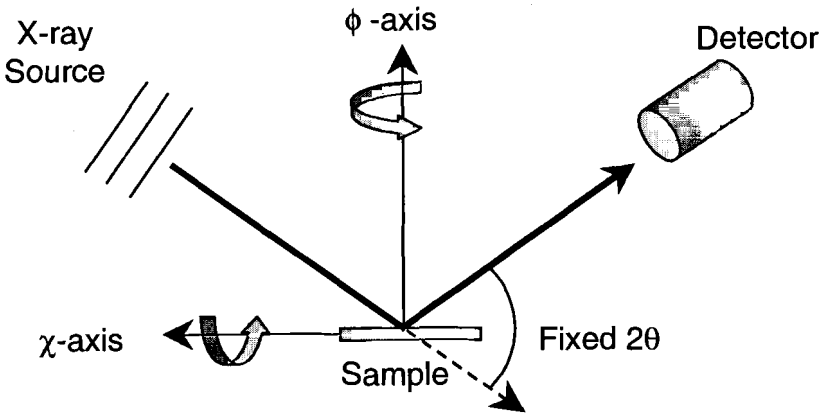


Figure 3.7: Schulz pole figure geometry.

accomplished by sample rotations about the $\phi$ and $\chi$ axes of a four-circle diffractometer, where the source and detector are maintained at a fixed $2\theta$. A contour map of the intensity is then plotted as a function of the angular orientation of the specimen. Pole figures are typically represented by a stereographic projection of the intensity measurements,[14] where the $\chi$ and $\phi$ parameters correspond to the radial and angular arguments, respectively, within a polar coordinate system.

### 3.4 Chapter References

[1] D. Briggs, M.P. Seah, Practical Surface Analysis By Auger and X-ray Photoelectron Spectroscopy, 2nd ed., Chichester: Wiley (1990).

[2] J. Chastain, Handbook of X-ray Photoelectron Spectroscopy, Eden Prairie: Perkin-Elmer (1992).

[3] J.R. Hook, H.E. Hall, Solid State Physics, 2nd ed., Chichester: Wiley (1991).

[4] M.A. Omar, Elementary Solid Sate Physics: Principles and Applications, Reading: Addison-Wesley (1975).

[5] Z.L. Wang, Reflection Electron Microscopy and Spectroscopy for Surface Analysis, Cambridge: Cambridge University Press (1996).

[6] D.B. Williams, C.B. Carter, Transmission Electron Microscopy, New York: Plenum Publishing (1996).

[7] M. Ohring, Materials Science of Thin Films, 2nd ed., London: Academic Press (2002).

[8] L.J. LeGore, O.D. Greenwood, J.W. Paulus, D.J. Frankel, R.J. Lad, "Controlled growth of $WO_3$ films", *J. Vac. Sci. Technol. A* 15 (1997) 1223-1227.

[9] K. Mae, V. Moshchalkov, Y. Bruynseraede, "Intensity profiles along the RHEED streaks for various thin film surface morphologies", *Thin Solid Films* 340 (1999) 145-152.

[10] S.C. Moulzolf, L.J. LeGore, R.J. Lad, "Heteroepitaxial growth of tungsten oxide films on sapphire for chemical gas sensors", *Thin Solid Films* 400 (2001) 56-63.

[11] F. Jona, J.A. Strozier Jr., W.S. Yang, "Low-energy electron diffraction for surface structure analysis", *Rep. Prog. Phys.* 45 (1982) 527-585.

[12] L.A. Aslanov, G.V. Fetisov, J.A.K. Howard, Crystallographic Instrumentation, New York: Oxford University Press (1998).

[13] L.G. Schulz, "A direct method of determining preferred orientation of a flat reflection sample using a geiger counter X-ray spectrometer", *J. Appl. Phys.* 20 (1949) 1030-1033.

[14] B.D. Cullity, Elements of X-ray Diffraction, 2nd ed., Reading: Addison-Wesley (1978).

# CHAPTER 4: THIN FILM SYNTHESIS AND CHARACTERIZATION FACILITY

Shown in Figure 4.1 is a schematic of the Thin Film Synthesis, Characterization and Processing Facility located in the Laboratory for Surface Science and Technology at the University of Maine. All of the ultra-high vacuum (UHV) chambers, including the interconnecting dual ion pumped trolley line, are capable of routinely achieving base pressures within the $10^{-10}$ torr range (1 atm = 760 torr). Sample transfer between the chambers is conducted *in vacuo* via a trolley line designed by DCA Instruments, Turku, Finland. This system allows for deposited films to be characterized by a variety of surface sensitive techniques before being exposed to air.

Samples are mounted onto flat disk-shaped metal carriers (e.g. tantalum or stainless

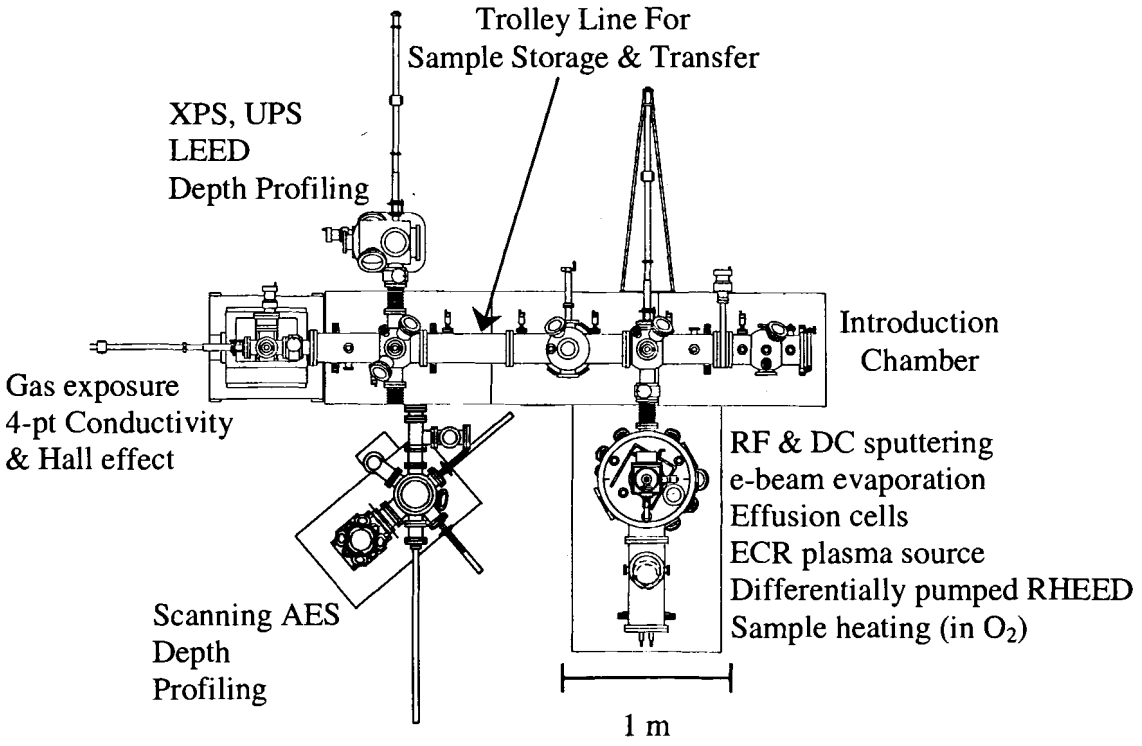


Figure 4.1: Top view of the thin film synthesis and characterization facility at LASST.

steel) that are 4.6 cm in diameter and 1.8 mm thick, and entered into the system via a turbo-pumped introduction chamber. Sample storage and transfer within the trolley line is accomplished with two 'trolley carts', each capable of holding up to 14 carriers with samples. By magnetically coupling internal gears with external manipulators, the carts can be linearly moved along the trolley line. Samples are transferred from the cart to a specific vacuum chamber manipulator by first extracting a sample from the cart with magnetically coupled pick-up manipulators, and then transferring the sample onto a horizontal transfer arm, which extends into the particular chamber for sample docking. The following sections describe two of the chambers (Deposition and Characterization) in detail.

In addition to the UHV characterization and processing facility, crystallographic orientation and lattice constant measurements were also obtained *ex-situ* with a Scintag four-circle X-ray diffractometer. The X-rays were provided by a 1.8 kW line focus, achromatic Cu K$\alpha$ source ($\lambda_{ave}$ = 1.5418 Å). Normal $\theta$-$\theta$ scans were performed with the Bragg-Brentano arrangement, and pole figure measurements were conducted in accordance with the Schulz geometry.

### 4.1 Deposition Chamber

Housed within the 60-cm diameter deposition chamber are a variety of thin film synthesis methods (see Figure 4.1). Figure 4.2 depicts several of the relevant aspects of the deposition chamber used in this study. A 6 kW Telemark four pocket (7 cc pocket size) electron beam evaporator was utilized to evaporate $WO_3$ 99.995% pure source material. Main chamber pumping is performed by a Varian 1,000 L/s turbo and Varian

ion pump, which can achieve a base pressure of ~ 5 x $10^{-10}$ torr after a 12 – 24 hour bake at 150 °C. Film deposition rates were measured *in situ* with a Leybold Inficon quartz crystal monitor (QCM), which was calibrated against total film thickness measurements obtained *ex situ* with a surface profilometer. Total film thickness measurements indicated that the measured QCM deposition rates for the $WO_3$ films required a 13.2% "tooling factor" correction due to the difference in location between the QCM and the sample plane with respect to the evaporator. Within the sample holder/manipulator, samples were radiantly heated with a boron nitride (BN) encased graphite heater. An S-type thermocouple located near the sample, which was calibrated against a thermocouple touching the sample carrier surface in a separate experiment, was utilized to determine substrate temperatures for different film growths. Process gases (e.g. $O_2$, $N_2$, and Ar) for plasma production, film growth, or other experimentation are connected to the chamber via MKS mass flow controllers.

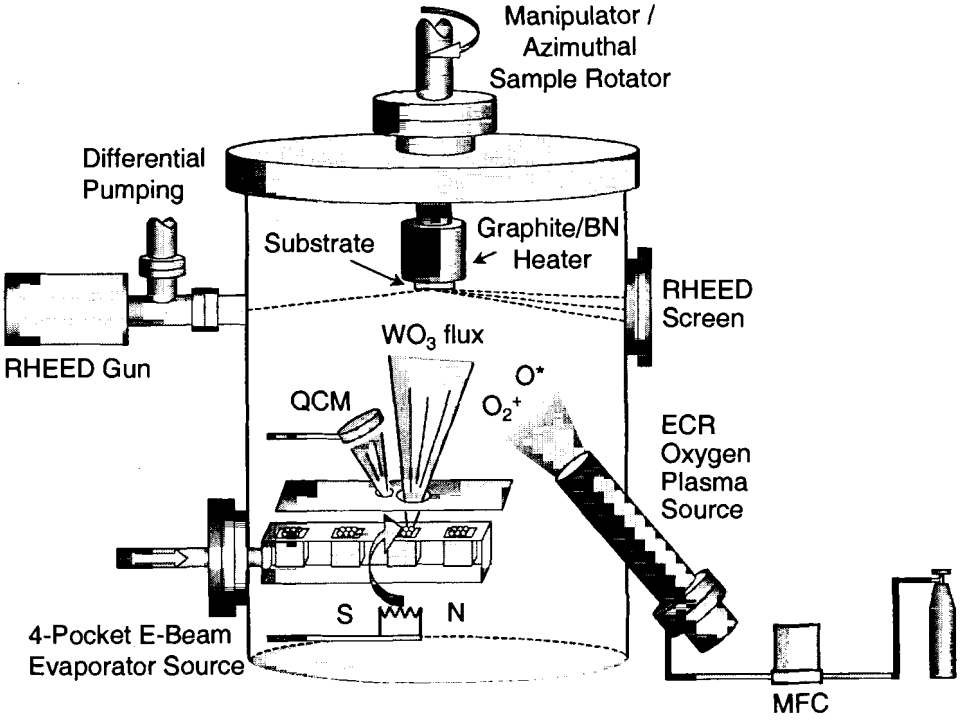


Figure 4.2: Side view of the deposition chamber.

The main chamber is also equipped with a Staib Instruments 30 keV RHEED gun and phosphor detection screen. A differential pump connected to the RHEED gun allows *in situ* measurements with oxygen partial pressures ranging up to $10^{-4}$ torr. The capture of diffraction images was accomplished with a CCD camera interfaced with K-Space KSA 400 data acquisition software coupled with a PXR800 frame grabber board.

A Wavemat Inc. electron cyclotron resonance (ECR) plasma source was used to produce an argon or oxygen plasma for both substrate processing/cleaning and assisted film growth. In the ECR plasma method, microwave energy (e.g. 2.45 GHz) is coupled with the natural resonant frequency of electrons in a tunable microwave cavity having one end open to the main chamber. In the presence of a static magnetic field provided by the ECR source module, electrons undergo cyclotron resonance and collide with gas atoms and/or molecules admitted into the cavity. For our experiments, $O_2$ gas was utilized for assisted film growth, and the ensuing electron collisions produced $O^*$ radicals as well as $O_2^+$ ions within the plasma. The resulting energy of these species is approximately 10 – 20 eV,[1] which can be dissipated upon collision with the substrate leading to enhanced surface diffusivity of the adsorbed atoms, thereby creating high quality films.[2,3]

### 4.2 Characterization Chamber

The surface characterization chamber shown in Figure 4.3 contains instruments for chemical and structural analysis of substrates and/or deposited films. The chamber is fitted with a SPECS PHOIBOS HSA 3000 Plus hemispherical energy analyzer and data acquisition software for XPS/UPS measurements and analysis. A VG dual-anode 300 W

source is capable of generating Mg Kα (1253.6 eV) and Al Kα (1486.6 eV) X-rays for core level electron analysis; the UV source provides photon energies from He I (21.2 eV) or He II (40.8 eV) glow discharges for valence band analysis. Sample heating is accomplished with the same type of graphite/BN heater used in deposition chamber.

Compositional depth profile analysis is accomplished with a differentially turbo-pumped SPECS IQE 12/38 ion gun mounted onto the characterization chamber. An argon process gas is utilized for ion generation, where ion accelerating potentials of up to 5 kV can be achieved. The ion gun is interfaced with SPECS data acquisition software that allows fully automated depth profile measurements to be obtained via XPS/UPS methods.

For surface structure analysis, the characterization chamber is equipped with a Vacuum Generators (VG) rear view LEED optics system. The three-mesh, phosphor

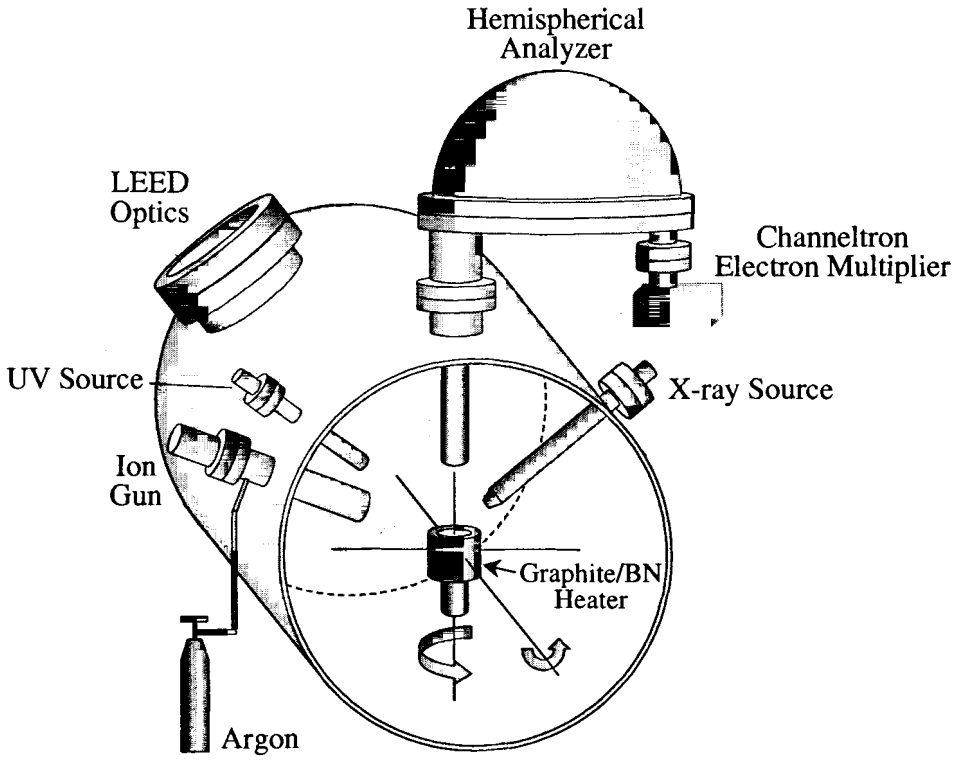


Figure 4.3: Side view of the surface characterization chamber.

detection screen assembly allows for the detection of elastically backscattered electrons, where the electron gun is capable of generating incident electron energies up to 1000 eV. Image capturing and analysis is accomplished with the CCD camera and software previously described for the RHEED system.

### 4.3 Chapter References

[1] MPDR 610I ECR Microwave Plasma Source product brochure, Wavemat, Inc. Plymouth, MI.

[2] J. Asmussen, "A review of ECR plasma processing technology", *IEEE International Conf. on Plasma Sci.* (1991) 139.

[3] L. J. LeGore, O. D. Greenwood, J. W. Paulus, D. J. Frankel, R. J. Lad, "Controlled growth of $WO_3$ films", *J. Vac. Sci. Technol. A* 15 (1997) 1223-1227.

# CHAPTER 5: CHARACTERIZATION AND ANALYSIS OF THE $BaF_2$ / Si SUBSTRATE

## 5.1 $BaF_2$/Si Sample Preparation

For this investigation, the NSWCDD research group provided a 3-inch Si (100) single crystal wafer upon which a 300 Å $BaF_2$ (111) thin film was deposited. Details concerning the $BaF_2$ deposition process can be found in the cited references.[1,2] Substrates of approximately 1 $cm^2$ were obtained for our studies by scribing the as received wafer along the Si {100} planes. The substrates were then mounted onto tantalum carriers by spot welding tantalum wire (0.008 inches in diameter) across the sample corners. This type of wire mount additionally served to electrically ground subsequent film growth upon the $BaF_2$ insulator layer, thereby reducing the charging effects induced by X-ray or electron-beam irradiation during various film characterization processes. Samples were blown with dry nitrogen before introduction into the UHV system so as to minimize large particle contaminants acquired during the mounting procedure. Once introduced into the deposition chamber, and prior to deposition, the substrates were processed with a 200 watt ECR argon plasma ($10^{-4}$ torr) for 20 minutes. XPS measurements before and after this processing indicated the removal of hydrocarbon and minimization of oxide contaminants (< 5 % – 10% oxygen concentration) from the substrate surface with no apparent damage to the $BaF_2$ thin film stoichiometry and microstructure as per XPS and diffraction studies.

## 5.2 Chemical and Structural Characterization of the $BaF_2$ Film Layer

Figure 5.1(a) shows a typical XPS wide scan spectrum from the $BaF_2$ film layer, and the inset 5.1(b) shows more detailed region scans of the $Ba3d_{3/2,5/2}$ and F1s photoelectron

peaks. Barium, fluorine, and oxygen account for all peaks within the wide scan, where no carbon contaminants could be detected post ECR processing. The peak positions for $Ba3d_{5/2}$ and F1s energy levels were measured at 781.7 eV and 685.8 eV, respectively, which correspond well with published values for $BaF_2$.[3,4] The O1s peak position is shifted by approximately 0.5 eV to higher binding energies as compared to the known energy level for atomic oxygen at 531.0 eV.[4] This shift is consistent with reports of adsorbed $O_2$ species on a barium surface,[5] as compared to energy shifts of approximately 1 to 2 eV in O1s that result from hydroxide formation.[4] XPS composition measurements consistently indicated an approximate 1:2 ratio for barium and fluorine, with oxygen contamination typically below 5% - 10%.

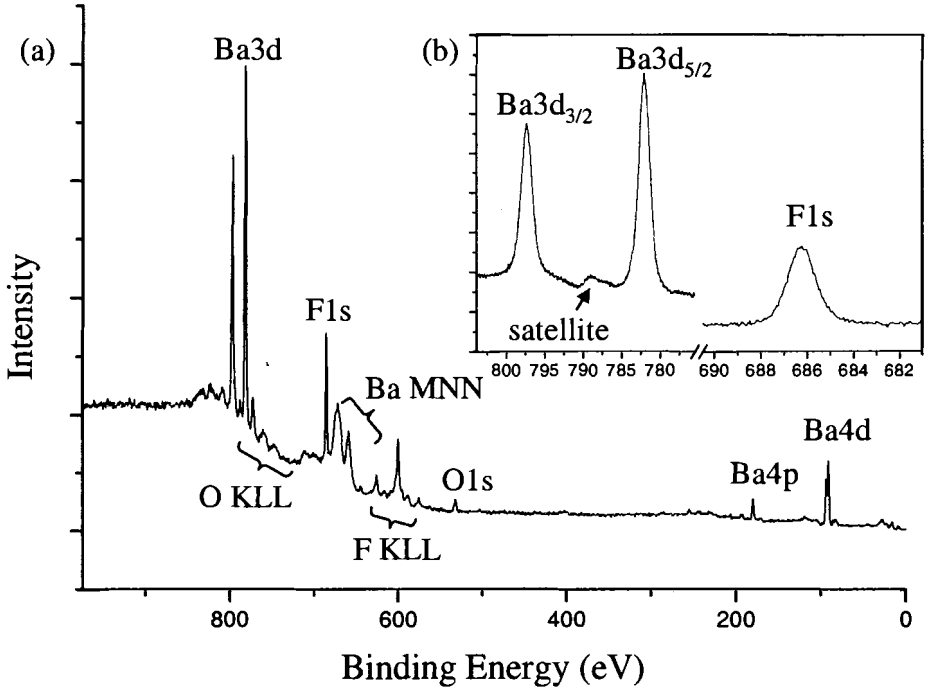


Figure 5.1 Typical XPS spectrum from the $BaF_2$ substrate surface. (a) wide energy scan, and (b) high resolution scans of the Ba and F binding energy peaks. The Mg $K\alpha_{3,4}$ satellite peak is indicated for $Ba3d_{3/2}$.

An XRD θ-θ measurement for the $BaF_2$ thin film, shown in Figure 5.2(a), reveals a strong peak at $2\theta = 24.9^\circ$ and a second order diffraction peak at $51.0^\circ$. The d-spacing for the $24.9^\circ$ peak corresponds to 3.58 Å, which agrees well with published values for bulk $BaF_2$ (111).[6,7] The pole figure in Figure 5.2(b) shows a series of peaks which correspond to the family of {200} poles for the $BaF_2$ film. To better understand the results of this pole figure measurement, we consider the following: for any (111) oriented single crystal cubic structure, XRD pole figure measurements about the ϕ-axis ( = [111]-direction for this cubic system) for a fixed $2\theta = \{100\}$ planes would satisfy the Bragg diffraction condition at specific ϕ angles when $\chi = 54.7^\circ$.

$$\text{i.e. } \chi = \cos^{-1}\left(\frac{[111] \bullet [100]}{\|[111]\| \, \|[100]\|}\right) = 54.7^\circ \qquad (5\text{-}1)$$

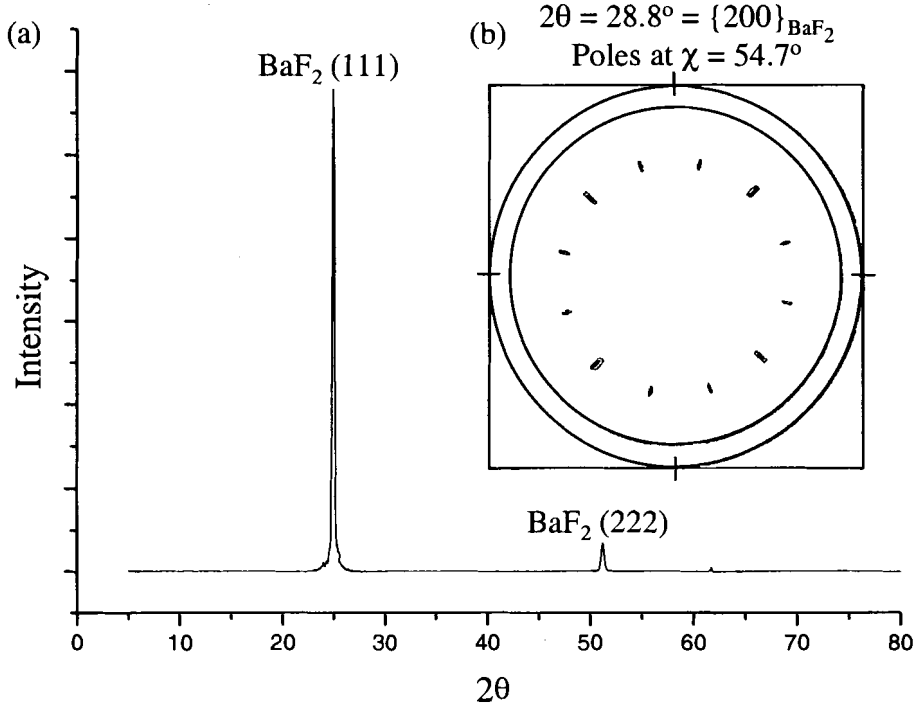


Figure 5.2 (a) XRD θ-θ scan and (b) pole figure of the $BaF_2$ (111) film layer.

This particular pole figure arrangement is graphically displayed in Figure 5.3, which relates the various cubic structure orientations with respect to the goniometer axes of the diffractometer. Specifically, at these 2θ and χ parameters, rotation about the ϕ-axis would render three peaks separated by 120°, corresponding to the (100), (010), and (001) planes, respectively (see Figure 5.3). However, in performing such a measurement on the $BaF_2$ substrate film, not three, but twelve peaks equally spaced in 30° increments about the ϕ-axis (see Figure 5.2(b)) were observed at these same 2θ and χ parameters This increase in the number of expected peaks can be explained by the presence of not one, but four distinct cubic domains existing within the $BaF_2$ film layer, differentiated by 30°

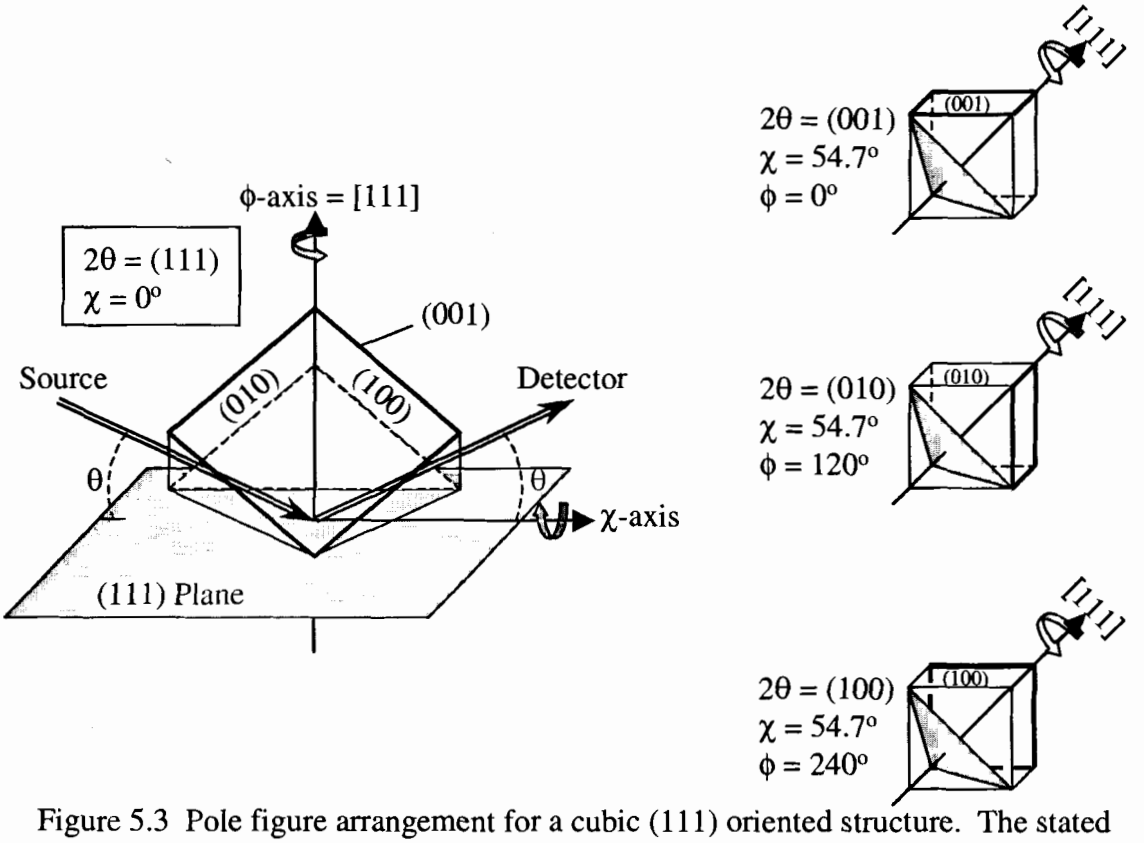


Figure 5.3 Pole figure arrangement for a cubic (111) oriented structure. The stated values for the 2θ, χ, and ϕ parameters for the three smaller cubes define when the Bragg condition is satisfied for measurement of the {100} poles. The (001) plane has a bold outline for clarification.

rotations about the [111]-axis. In such a distribution, one particular domain would satisfy the Bragg condition at 0, 120°, and 240° about $\phi$; a second domain at 30°, 150°, and 270°; a third domain at 60°, 180°, and 300°; and a fourth domain at 90°, 210°, and 330°.

Due to the four equivalent crystallographic domains, it would be reasonable to expect the grown $BaF_2$ film to exhibit morphology that reflects the different singly oriented clusters, or grains. Such formations result from island (or Volmer-Weber) or Stranski-Krastanov growth modes, which are common deposition modes for metal-metal and metal-semiconductor systems.[8] Evidence of these grains can be seen in a contact mode atomic force microscope (AFM) image taken from the $BaF_2$ substrate film (Figure 5.4), where relatively smooth regions (rms roughness ~ 8 Å) of size approximately 500 nm $\times$500 nm are separated by well-defined boundaries.

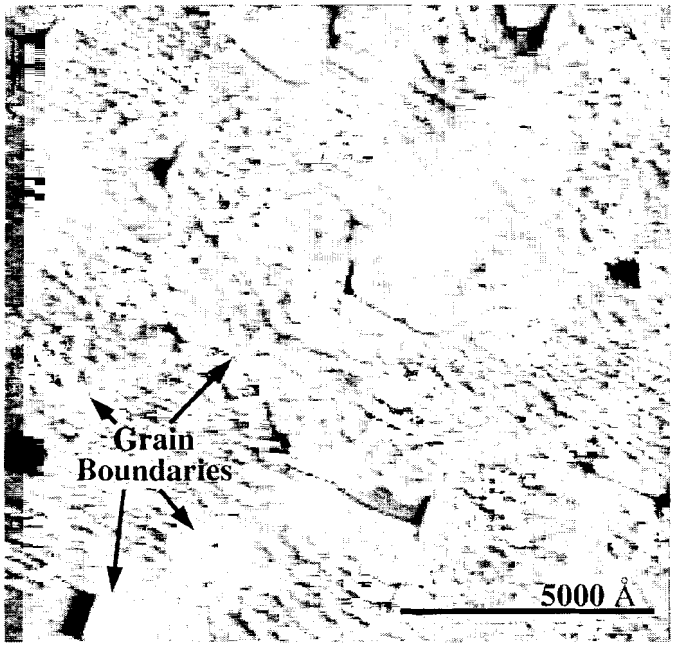


Figure 5.4 AFM image of the $BaF_2$ substrate indicating a surface composed of relatively smooth grains (rms roughness ~ 8 Å) separated by well defined grain boundaries.

### 5.3 The $BaF_2$ Surface Mesh

When considering $BaF_2$/Si as a platform for subsequent film growth, we can idealize the growth surface, or surface mesh, to be the set of $BaF_2$ (111) planes parallel to the Si (100) substrate. In particular, when bulk terminated along the (111) $BaF_2$ planes, the four cubic orientations in 3-D reduce to two distinct hexagonal plane orientations offset by 30° in 2-D. This is illustrated in Figure 5.5 by the top down view of the four cubic orientations along the [111] axes. The cubic orientations labeled I and III in the figure produce identically oriented 2-D hexagonal surface mesh structures within their (111) planes; and a similar correspondence occurs for the 3-D orientations labeled II and IV.

This surface mesh crystallography was verified by both RHEED and LEED patterns taken from the $BaF_2$ film surface. For the RHEED patterns, absolute reciprocal distance measurements were calculated through the use of calibration measurements obtained

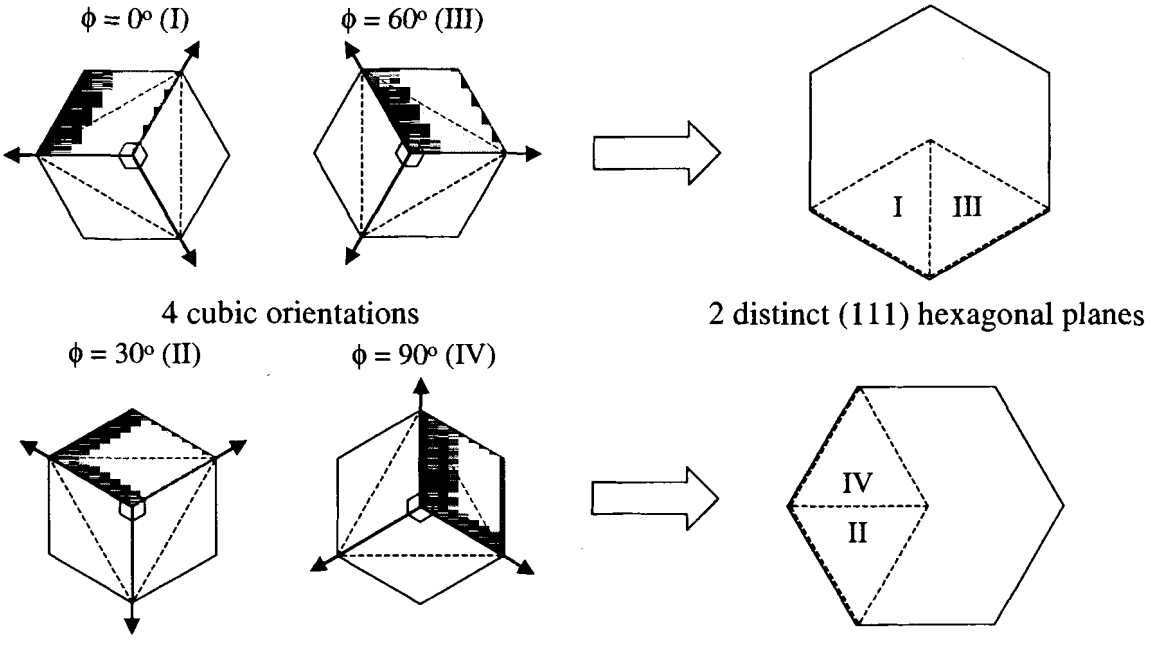


Figure 5.5 A top down view of the four $BaF_2$ cubic structure orientations (i.e. [111] axes through page). The dashed triangles indicate the (111) planes. When bulk terminated along the (111) planes, two distinct hexagonal meshes are produced.

from basal oriented single crystal sapphire (i.e. the $\alpha$-$Al_2O_3$ (00•1) surface). From the known lattice constant of 4.76 Å for basal sapphire, a camera constant $\kappa$ (units of $Å^{-1}$/ # pixels) was obtained. From this calibration, we were able to determine that the lateral spacings within the $BaF_2$ RHEED pattern (Figure 5.6(a)), which repeated every 30° upon sample rotation, were a superposition of two distinct surface mesh domains. Specifically, the $d_1^*$ lateral spacing in the RHEED pattern corresponded to the case where the RHEED beam was parallel to $[11\bar{2}]_{BaF_2}$, and the $d_2^*$ lateral spacing corresponded to where the RHEED beam was parallel to $[\bar{1}10]_{BaF_2}$, or equivalently $[10\bar{1}]_{BaF_2}$ (see Figure 5.6(b)).

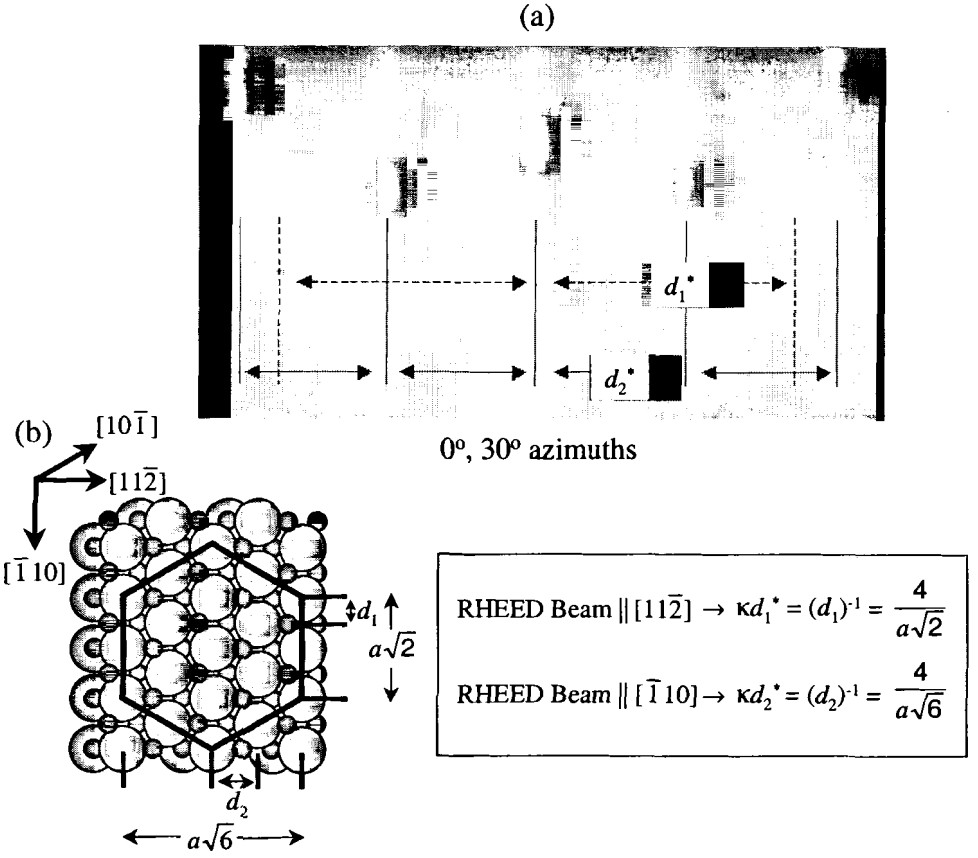


Figure 5.6 (a) 30 keV RHEED pattern for the $BaF_2$ surface, where the reciprocal lateral space distances $d_1^*$ and $d_2^*$ are shown. (b) A ball model of the $BaF_2$ (111) surface relating the reciprocal lattice space distances $d_1^*$ and $d_2^*$ in (a) with their real space distances $d_1$ and $d_2$ in terms of the lattice constant $a$. The large and small spheres in the model correspond to Ba and F atoms, respectively.

For RHEED patterns obtained in this study, the effective surface area of the sample analyzed within a given RHEED pattern corresponds to the electron beam width (approximately 100μm), and length (approximately 1 mm) in the direction of the incident beam resulting from the grazing incidence angle between the beam and sample. Since this analyzed surface area is much larger than the apparent average grain size observed in the AFM images of the $BaF_2$ surface (approximately 500 $nm^2$), a superposition of multiple surface domains within the diffraction pattern is to be expected. In addition, the presence of vertical streaks within the RHEED spot profile were indicative of long range order existing in a direction parallel to the surface as compared to the surface normal direction. This qualitative assessment corresponds well with the AFM observations, which indicated a surface dominated by relatively smooth grains.

Perhaps even more revealing than the RHEED data were the LEED patterns of the $BaF_2$ surface structure (Figure 5.7(a)), which clearly shows a superposition of two hexagonal surface meshes in reciprocal/real space offset by 30°. (For 2-D hexagonal systems, the geometry of the hexagonal mesh is maintained in both real and reciprocal space – the only difference, other than magnitude, is a 30° in-plane offset. The conversion equations from real to reciprocal space in a 2-D system are the same as the 3-D conversions for $\vec{a}^*$ and $\vec{b}^*$ in Equation 3-10, except $\vec{c}$ now becomes the unit normal $\hat{n}$ of the plane defined by $\vec{a}$ and $\vec{b}$.) As with RHEED, the larger LEED electron beam width samples multiple surface domains, and hence a superposition of diffraction events from both domains is observed.

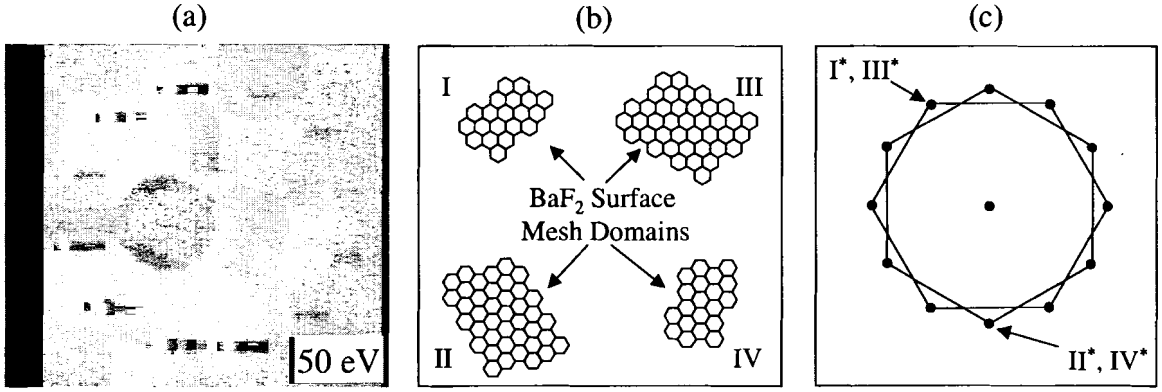


Figure 5.7 (a) 50 eV LEED pattern from the $BaF_2$ surface. (b) A model of the $BaF_2$ surface mesh illustrating how the film is composed of grains possessing two distinct surface mesh orientations. The I through IV labels are consistent with the four distinct cubic orientations in Figure 5.5. (c) A superposition of the reciprocal space surface mesh domains in (b).

By assimilating all of the morphological and crystallographic data discussed, we have developed a model of the $BaF_2$ surface mesh structure which will act as the template for subsequent film growth, as illustrated in Figure 5.7(b). To summarize, the four distinct grain orientations within the $BaF_2$ film layer reduce to two distinct hexagonal surface mesh platforms. The combined effect of the two hexagonal mesh platforms results in a surface mesh that maintains $30^o$ in-plane rotation symmetry. This symmetry is illustrated by superimposing the reciprocal space domains in Figure 5.7(b), as illustrated in Figure 5.7(c), which accurately predicts the observed LEED pattern in Figure 5.7(a).

## 5.4 Chapter References

[1] F. Santiago, D. Wood, T. K. Chu, C. A. Huber, "Interface characterization of PbTe/BaSi/Si heterostructures grown using MBE", *Mater. Res. Soc. Symposium Proc.* 281 (1993) 603-608.

[2] T. K. Chu, F. Santiago, M. Stumborg, C. A. Huber, "The role of barium in the heteroepitaxial growth of insulator and semiconductors on silicon", *Mater. Res. Soc. Symposium Proc.* 334 (1994) 501-506

[3] H. Seyama, M. Soma, *J. Chem. Soc. Faraday Trans. I* 80 (1984) 237.

[4] J. Chastain, Handbook of X-ray Photoelectron Spectroscopy, Eden Prairie: Perkin-Elmer (1992).

[5] M. Ayyoob, M. S. Hegde, *J. Chem. Soc. Faraday Trans. I* 82 (1986) 1651.

[6] R. W. G. Wyckoff, Crystal Structures, 2nd ed., Vol. 1, New York: Wiley (1964).

[7] JCPDS International Centre for diffraction Data (1997).

[8] M. Ohring, The Materials Science of Thin Films, 2nd ed., London: Academic Press (2002).

# CHAPTER 6: CHARACTERIZATION AND ANALYSIS OF $WO_3$ FILM GROWTH AND $BaWO_4$ INTERFACIAL REACTION LAYER FORMATION

## 6.1 $WO_3$ Film Deposition Parameters

The resultant microstructure of a grown thin film strongly depends not only on the substrate structure, but also on the deposition method and the growth conditions. All films discussed in this thesis were deposited via electron-beam evaporation of a 99.995% pure $WO_3$ source to a total thickness of 50 nm. The growth condition parameters at our disposal included substrate temperature, $O_2$ flow rate, deposition rate, deposition pressure, and the presence of an oxygen plasma to assist the deposition process. For all $WO_3$ films grown in our studies, only the substrate temperature was varied. Experiments were performed at room temperature to approximately 650°C, where $BaF_2$ is known to dissociate and form $BaSi_2$ with the silicon substrate at approximately 700°C.[1] All other deposition parameters were held fixed, which included an $O_2$ flow rate of 5 standard cubic centimeters per minute (sccm), deposition rate of 0.2 Å/s, and deposition partial oxygen pressure of $10^{-4}$ torr. In addition, film depositions were assisted by a 200 watt powered ECR $O_2$ plasma to enhance the surface diffusivity of the adsorbed oxygen species as well as to ensure that excess oxygen was present to yield stoichiometiric $WO_3$. The selection of the fixed deposition parameters was in large part based upon the success others have experienced in producing high quality, epitaxial grade $WO_3$ thin films on sapphire substrates.[2,3]

## 6.2 Chemical Analysis of the $WO_3$ Film Layer

Table 6.1 summarizes the XPS results for $WO_3$ films that were deposited at substrate temperatures ranging from 350 to 550°C. In particular, the measured binding energy for

Table 6.1 - XPS measurements from $WO_3$ films grown at different temperatures

| Substrate Temp (°C) | Binding Energy ; FWHM (eV) | | Peak Area Ratio | Doublet Sep. |
|---|---|---|---|---|
| | $W4f_{7/2}$ | O1s | $O1s/W4f_{7/2}$ | W4f (eV) |
| 350 | 35.9 ; 1.20 | 530.9 ; 1.48 | 2.65 | 2.1 |
| 400 | 35.8 ; 1.16 | 530.8 ; 1.42 | 2.95 | 2.2 |
| 450 | 35.8 ; 1.18 | 530.7 ; 1.44 | 2.95 | 2.1 |
| 500 | 36.0 ; ----- | 530.9 ; ----- | 3.18 | 2.1 |
| 550 | 35.8 ; 1.13 | 530.7 ; 1.42 | 3.20 | 2.1 |

the $W4f_{7/2}$ peak ranged from 35.8 to 36.0 eV, where the $4f_{5/2,7/2}$ doublet separation was approximately 2.1 eV in all cases. The measured binding energy for the O1s orbital ranged from 530.7 to 530.9 eV. All of these measured peak positions and 4f doublet separations correspond well to those reported for $WO_3$.[4,5] Furthermore, high resolution spectra of the W4f doublet indicated that the tungsten atoms primarily reside within the fully oxidized, $W^{+6}$ oxidation state. Evidence for this is seen in Figure 6.1(a), which shows representative W4f and O1s spectra of films that were deposited over the entire substrate temperature range. The highly symmetric nature of these peaks is indicative of a single bonding state. If multiple oxidation states had been present, the combined effect of reduced (i.e. $W^{+6-\delta}$) and fully oxidized tungsten species would broaden and distort this symmetry due to the presence of lower binding energy states (e.g. approximately 1 to 2 eV lower for $W^{+5}$ and $W^{+4}$). These findings are consistent with O1s to $W4f_{7/2}$ peak area ratio measurements for substrate temperatures of 400°C and 450°C, which indicate the correct 3:1 oxygen to tungsten ratio. For higher or lower substrate temperatures, there were slight deviations from the 3:1 ratio, which correspond to either oxygen deficient or oxygen excessive films.

To explain these slight stoichiometric deviations from $WO_3$, we first consider the oxygen deficient film grown at 350°C. Although reduced peaks could not be resolved

within the W4f doublet, the slightly broader full width at half max (FWHM) measurements for the $W4f_{7/2}$ and O1s peaks did suggest that a small component of reduced tungsten resided within this film as compared to the FWHM measurements for films grown at higher temperatures (see Table 6.1). The presence of a reduced tungsten component would therefore be consistent with the concentration ratio calculations for this particular film growth temperature.

For substrate temperatures ranging from 350 to 450°C, all peaks within the XPS spectrum could be accounted for by either tungsten or oxygen; Figure 6.1(b) shows a representative survey spectrum for films grown within this temperature range. However,

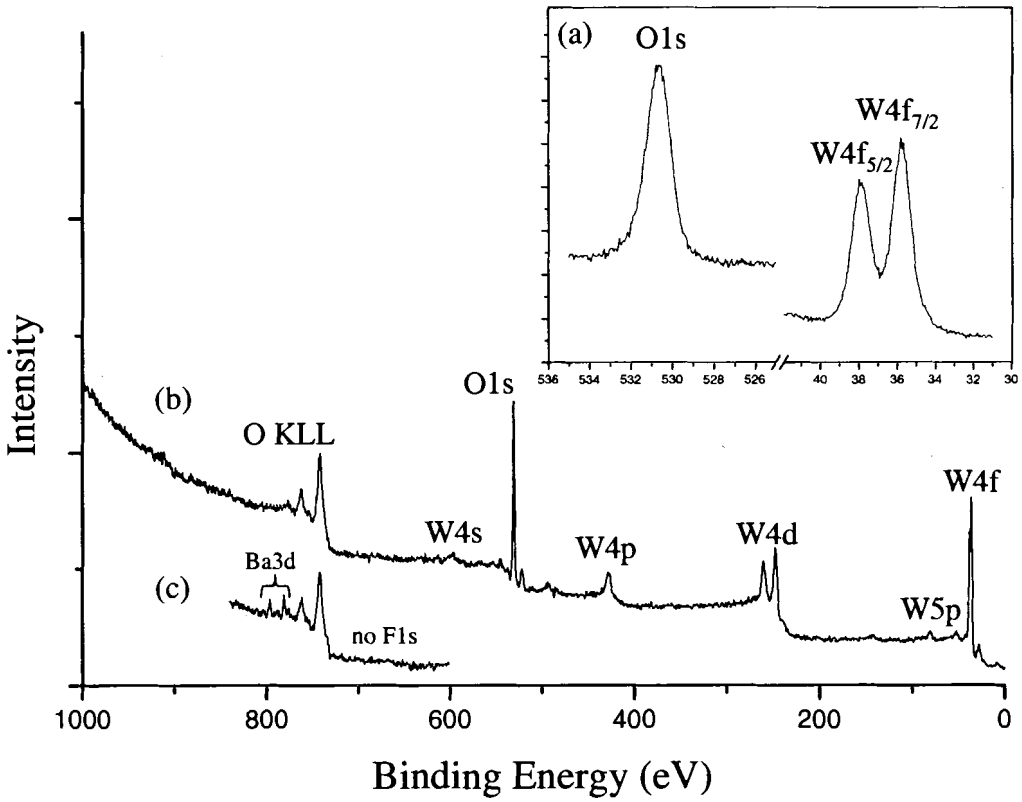


Figure 6.1 XPS spectra from $WO_3$ films. (a) High resolution scans of the O1s and W4f binding energy peaks. (b) Representative survey spectrum from films deposited over the range room temperature to 450°C. (c) Representative scan from films deposited in the range 500-550°C.

for growth between 500 and 550°C, a small Ba3d component, without a corresponding F1s peak, began to emerge, as shown in Figure 6.1(c). Although this XPS signal resulted in a total barium concentration of less than 1% for both the 500 and 550°C films, the formation of an oxidized barium compound layer at the $WO_3$ / $BaF_2$ interface could explain the excess oxygen measured in these films. Specifically, if a small percentage of the measured O1s photoelectrons were emerging from a film layer beneath a pure $WO_3$ layer, where this second layer additionally possessed an oxygen to tungsten ratio that was greater than 3:1 (e.g. $BaWO_4$), then the measured O1s/W4$f_{7/2}$ ratio would be greater than 3:1 as well. Although merely speculation at this point, evidence of this additional layer is presented in the next section, thereby substantiating this hypothesis for the apparent excess in oxygen within these films.

### 6.3 Structural Analysis of the $WO_3$ / $BaWO_4$ Film Layers

Contained in Figure 6.2 are various RHEED transmission patterns from the $WO_3$ films that show the effects of substrate growth temperature on the film microstructure. For substrate temperatures between room temperature and 350°C, $WO_3$ films yielded diffuse and faint bands within the RHEED patterns as seen in Figure 6.2(a). Such diffuse diffraction patterns result from amorphous or very finely grained polycrystalline film structures that randomly scatter the RHEED beam. However, for substrate temperatures ranging from 400 to 500°C, RHEED transmission patterns revealed the presence of highly ordered film structures. Figure 6.2(c) shows a representative RHEED pattern for this temperature range, where azimuthal sample rotations produced the same pattern every 30°. A line intensity profile along the top row of spots in Figure 6.2(c) is shown in Figure

6.2(d), which indicates a superposition of multiple peak intensities within the diffraction spots. This fine structure within the RHEED pattern is consistent with the superposition of multiple crystalline domains of nearly equal lattice spacing. Conversion from reciprocal to real space indicated that these patterns result from monoclinic, orthorhombic, and/or triclinic lattice structures of $WO_3$, which are all nearly cubic in nature and have similar lattice constants to within a few tenths of an angstrom (see Table 2.1). Since the bulk form of the triclinic structure is known to only be stable over much lower temperature ranges (-50 to 17°C), this phase was ruled out, leaving the possible structures to be the monoclinic and/or orthorhombic phase $WO_3$. Further distinctions

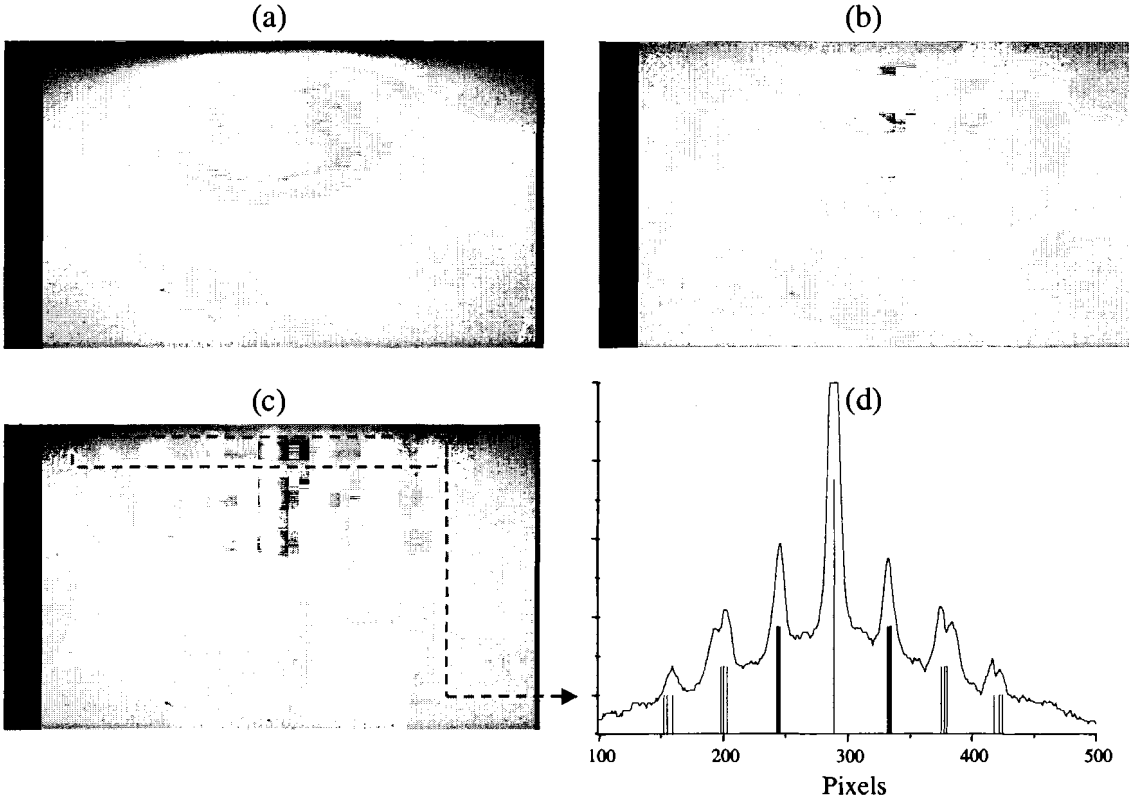


Figure 6.2 30 keV RHEED transmission patterns from $WO_3$ films deposited at (a) 350°C, (b) 550 °C, and (c) 400-500°C. (d) A line intensity profile along the row of spots shown in (c). Distances between the peaks have been fitted with the relative reciprocal space distances for the (002), (020), and (200) inter-planer spacings of monoclinic phase $WO_3$, which are represented by the vertical lines along the horizontal axis.

between these phases and cubic face orientations could not be resolved in the RHEED data due to the extremely small differences in lattice constants within and between the monoclinic and orthorhombic structures. To illustrate this point, vertical lines have been placed along the horizontal axis in Figure 6.2(d) which show the fitted reciprocal space distances for the bulk monoclinic phase (002), (020), and (200) inter-planar spacings. For clarity, only the reciprocal space distances for the monoclinic phase are shown since the same set of planes for the orthorhombic phase produce nearly identical spacings.

Further increases in substrate temperatures (i.e. $\geq$ 550°C) rendered RHEED patterns consistent with that seen in Figure 6.2(b). The superimposed faint spots and ring patterns seen in Figure 6.2(b) indicate that films deposited in this temperature regime contain mixtures of polycrystalline and epitaxial components.

To gain further insight into the structural development of the $WO_3$ films, XRD $\theta$-$\theta$ measurements were conducted for the same samples analyzed by RHEED. A compilation of this data is presented in Figure 6.3, which outlines five Intensity vs. $2\theta$ plots for the films grown from 350 to 550°C range. Consistent with the RHEED data, the 350°C film showed no sign of crystalline film structure other than the $BaF_2$ (111) substrate peak. However, at 400°C, film structure begins to emerge, which is evidenced by additional peaks at $2\theta = 23.1^\circ$ and $26.4^\circ$. With increased substrate temperatures of 450°C, 500°C, and 550°C, Figure 6.3 indicates the eventual coexistence of three peaks at $23.1^\circ$, $23.6^\circ$, and $24.2^\circ$, which were identified as the monoclinic and/or orthorhombic $WO_3$ phase orientations of (002), (020), and (200), respectively. (For simplicity, the above film structure will be referred to as monoclinic only from this point forward, since the nearly identical lattice parameters for monoclinic and orthorhombic phases of $WO_3$

could not be distinguished within the error limits of our measurements.) In addition to the monoclinic $WO_3$ triplet and the $BaF_2$ (111) substrate peak at 24.9°, the θ-θ scans also reveal a relatively strong peak at 26.4° for substrate temperatures of 400°C or greater. Although several phases of low index $WO_3$ d-spacings correspond to this 2θ measurement, subsequent structural analysis revealed that this peak did not belong to any phase of $WO_3$, but resulted from the formation of tetragonal phase barium tungstate, or $BaWO_4$, having a (112) orientation (see Figure 6.6(a) for bulk lattice model). Furthermore, with the exception of the trace amounts of barium that were identified in the 500 and 550°C films, XPS studies indicated that the film surfaces consisted of tungsten and oxygen species only. From this, we could deduce that formation of $BaWO_4$ was

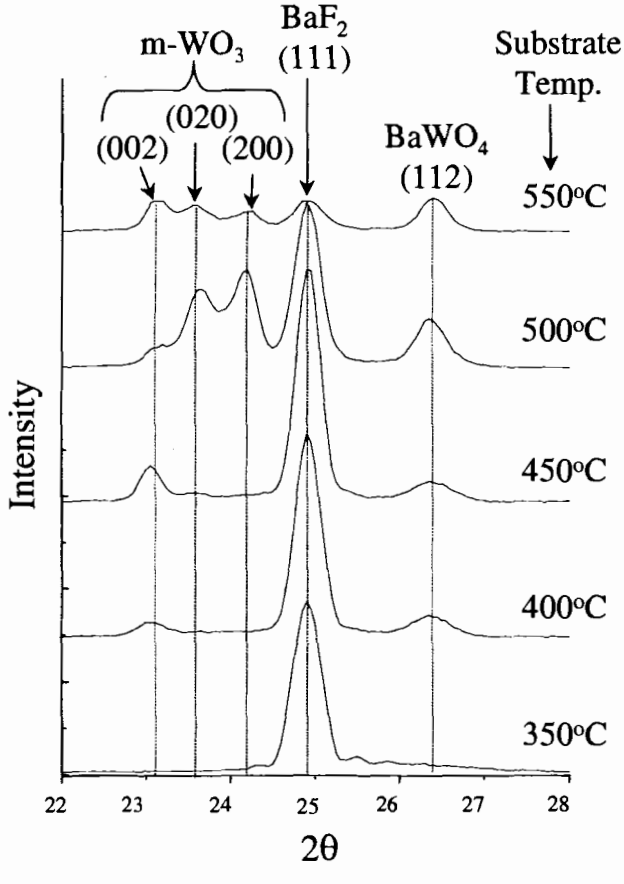


Figure 6.3 XRD θ-θ scans for $WO_3$ films deposited at the indicated temperatures.

most likely occurring at the interface between the $WO_3$ film and $BaF_2$ substrate. In addition, consistent with the RHEED observations, $WO_3$ film structures appeared to become compromised at the substrate temperature of 550°C, which was indicated by the intensity drop for these corresponding peaks in the θ-θ measurement. This failure of the deposited film to produce and/or maintain structural integrity at higher temperatures was presumably due to the aforementioned reactions between the $BaF_2$ film layer and the silicon substrate to form BaSi at these elevated temperatures. Such transformations within the $BaF_2$ film would likely disrupt the existing surface mesh matrix, thereby affecting its heterepitaxial relationship with the $WO_3$ layer. Indeed, for a substrate temperature of 650°C, XRD measurements (not shown) indicated the complete absence of the $BaF_2$ (111) structure as well as the lack of a structured $WO_3$ layer. Stumborg *et al*[6] have reported similar non-adherence of MBE grown films on $BaF_2$ (111)/ Si (100) substrates over this temperature range.

In order to uniquely determine the particular structural phases of $WO_3$ and $BaWO_4$, the θ-θ scans alone in Figure 6.3 could not completely provide the requisite information since a significant overlap exists for many low index planes among several phases of $WO_3$ for the region of interest (i.e. $2\theta \sim 23^\circ - 27^\circ$).[7,8] However, it was possible with XRD pole figure measurements to completely determine the dominant lattice structure domains within the film. The reason for this is due to the fact that, not only 2θ, but χ and φ parameters must also be correct to satisfy the Bragg condition for a particular set of planes associated with a particular lattice structure. The structural uniqueness provided by these three parameters, along with a material knowledge of the film/substrate system,

significantly reduces the possible candidates for the film structure, and in most cases to just one possible candidate.

With this in mind, pole figure measurements were performed on all grown films that exhibited the presence of lattice structure via RHEED and XRD θ-θ measurements. In particular, Figure 6.4(a) shows a pole figure that was conducted for the identification of monoclinic $WO_3$ by setting $2\theta = 34.2^\circ$, which corresponds to the (202) plane of m-$WO_3$. Twelve peaks, equally spaced about the azimuthal $\phi$ angle, were measured at a polar angle of $\chi = 46^\circ$, which was the expected polar angle displacement between the (002) and (202) planes for monoclinic $WO_3$. Similar pole figure measurements (not shown) for the monoclinic $WO_3$ (020) and (200) orientations in the θ-θ scan also revealed twelve peaks at the appropriate $\chi$ angles for the (220) and (202) planes, respectively.

Confirmation of (112) oriented $BaWO_4$ was also established by performing pole figure measurements. In Figure 6.4(b), $2\theta$ was set to $31.9^\circ$, corresponding to the {200} set of

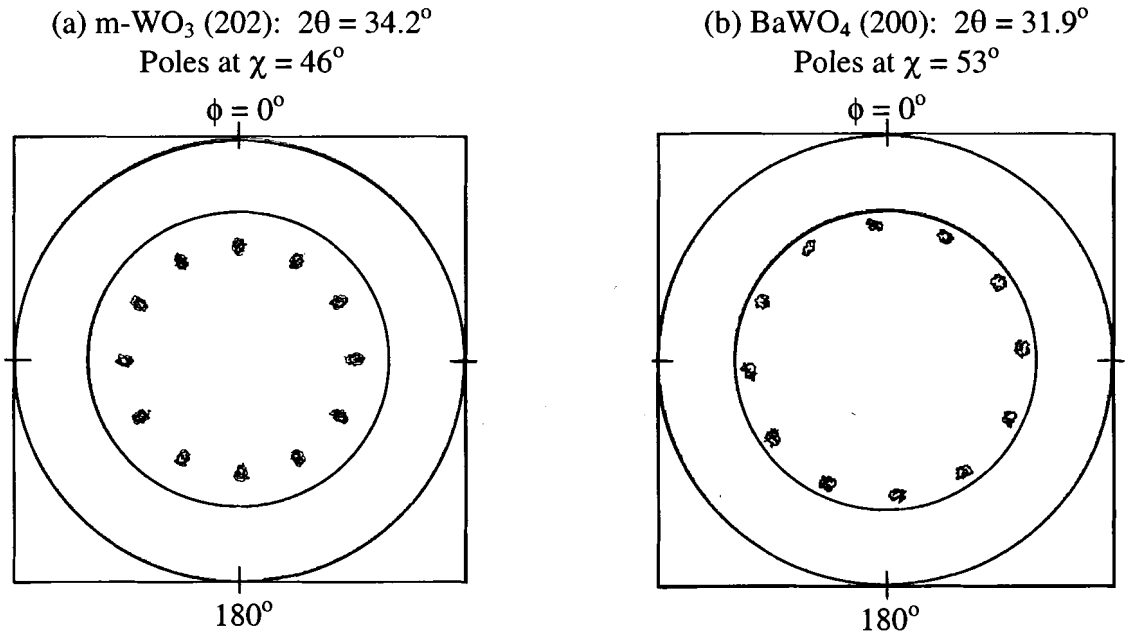


Figure 6.4 XRD pole figures measured from the (a) m-$WO_3$ film and (a) $BaWO_4$ film layers.

planes for $BaWO_4$. Again, twelve equally spaced peaks in $\phi$ appeared at a polar angle of $\chi = 53^\circ$, which agrees with the expected angle between the (112) and {200} planes of tetragonal $BaWO_4$. It is worth noting that, although the (200) and (020) planes have equal $2\theta$ and $\chi$ parameters within the pole figure for $BaWO_4$ in Figure 6.4(b), the difference in $\phi$ is not exactly $120^\circ$ as would be the case for a cubic-like structure, but is about $124.2^\circ$. The reason for this is because the *c* lattice parameter (= 12.7 Å) is slightly larger than $2a$ (= $2 \times 5.6$ Å) for $BaWO_4$, where $c = 2a$ would have produced an exact $120^\circ$ difference in $\phi$. The net result is an overall misalignment of approximately $4.2^\circ$ in $\phi$ within the measured peaks of Figure 6.4(b) for the (200) and (020) poles. A high-resolution $\phi$-scan at these $2\theta$ and $\chi$ settings shown in Figure 6.5 illustrates this slight discrepancy, revealing the doublet nature of the twelve peaks in the pole figure of Figure 6.4(b). A more detailed explanation of this high symmetry in the pole figures is given in section 6.4.

## 6.4 Substrate Symmetry and Lattice Match Considerations for $WO_3$ and $BaWO_4$ Formation

To understand why twelve peaks occur in the pole figures for both $WO_3$ and $BaWO_4$, we recall that the underlying $BaF_2$ (111) substrate surface mesh maintains an overall $30^\circ$ in-plane symmetry. Assuming that this surface mesh initially mediates the subsequent film structure, then the symmetry that exists within the surface mesh will be the overall symmetry translated into the primary film growth plane. For the $BaWO_4$ layer, this results in the formation of twelve distinct crystalline domains such that each domain is (112) oriented and possesses one of twelve possible orientations about the $[112]_{BaWO_4}$

axis. In other words, if the $BaWO_4$ layer was a single crystal specimen, then only one pair of peaks (e.g. 1 and 1' in Figure 6.5) would have been measured. The fact that twelve pairs of peaks were measured can therefore only be explained by the presence of twelve distinct single crystal domains. The $\phi$-scan in Figure 6.5 illustrates these twelve domains for the $BaWO_4$ layer, where the unprimed and primed labels correspond to the 124.2° separation between the (200) and (020) planes within a single domain.

Since the $WO_3$ structure is monoclinic, then, strictly speaking, the only explanation for the twelve measured peaks in the $WO_3$ pole figure is the existence of twelve distinct crystalline domains within this film layer as well. However, as previously mentioned, m-$WO_3$ is very nearly cubic, such that a single domain of a similarly oriented cubic lattice

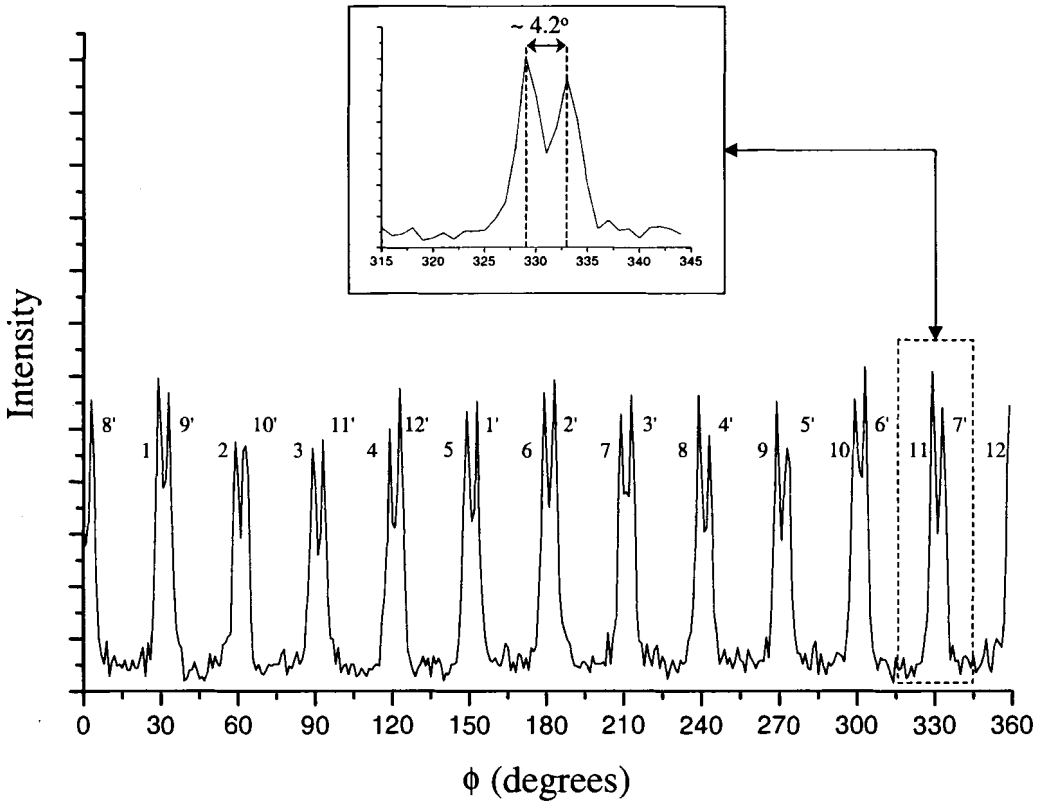


Figure 6.5 XRD $\phi$-scan from the $BaWO_4$ layer. Every pair of unprimed and primed numbers (e.g. 1 and 1') correspond to the (200) and (020) planes of a distinct $BaWO_4$ grain orientation about the $\phi$-axis (= $[112]_{BaWO_4}$).

would produce four peaks separated by 90° in this pole figure, corresponding to the (202), (022), $(\bar{2}02)$, and $(0\bar{2}2)$ poles of the cubic structure. Slight deviations from cubic, such as the case for m-$WO_3$, would then produce small changes in the $2\theta$, $\chi$, and/or $\phi$ parameters at which the poles are measured. Although such deviations were large and therefore distinguishable within the $BaWO_4$ $\phi$-scan as shown in Figure 6.5, such fine structure could not be resolved within the error limits of our diffractometer for the m-$WO_3$ pole figure.

To see why the $BaF_2$ surface mesh influences the specific film orientations, we consider the in-plane lattice misfits between $BaWO_4$ (112) and $BaF_2$ (111), and between $WO_3$ (002), (020), (200) and $BaWO_4$ (112). Figure 6.6(a) shows the $BaF_2$, $BaWO_4$, and m-$WO_3$ lattice structures with the corresponding interfacial planes; Figures 6.6(b) and 6.6(c) illustrate the lattice match schematics for the $BaWO_4$ / $BaF_2$ and $WO_3$ / $BaWO_4$ interfaces. To calculate the lattice misfit `f`, we utilized the following expression:[9]

$$f = \frac{[ma_o(s) - na_o(f)]}{na_o(f)}, \quad m,n = \text{integers} \tag{6-1}$$

where $a_o(f)$ and $a_o(s)$ refer to the film and substrate bulk lattice parameters, respectively. Equation 6-1 is a modified form of that given by Ohring[9] which does not include the $m,n$ factors. Their inclusion here allows for misfit calculations to be performed over an integral number of lattice parameters other than the limiting case of $m,n = 1$. (The determination of the $m,n$ values for a specific calculation is based upon the minimization of `f` for a given set of interfacial planes.) Table 6.2 shows the results of these various misfit calculations for all of the possible in-plane combinations at the two interfaces. We see that a smaller overall misfit exists at the $WO_3/BaWO_4$ interface (0.66% – 5.2%)

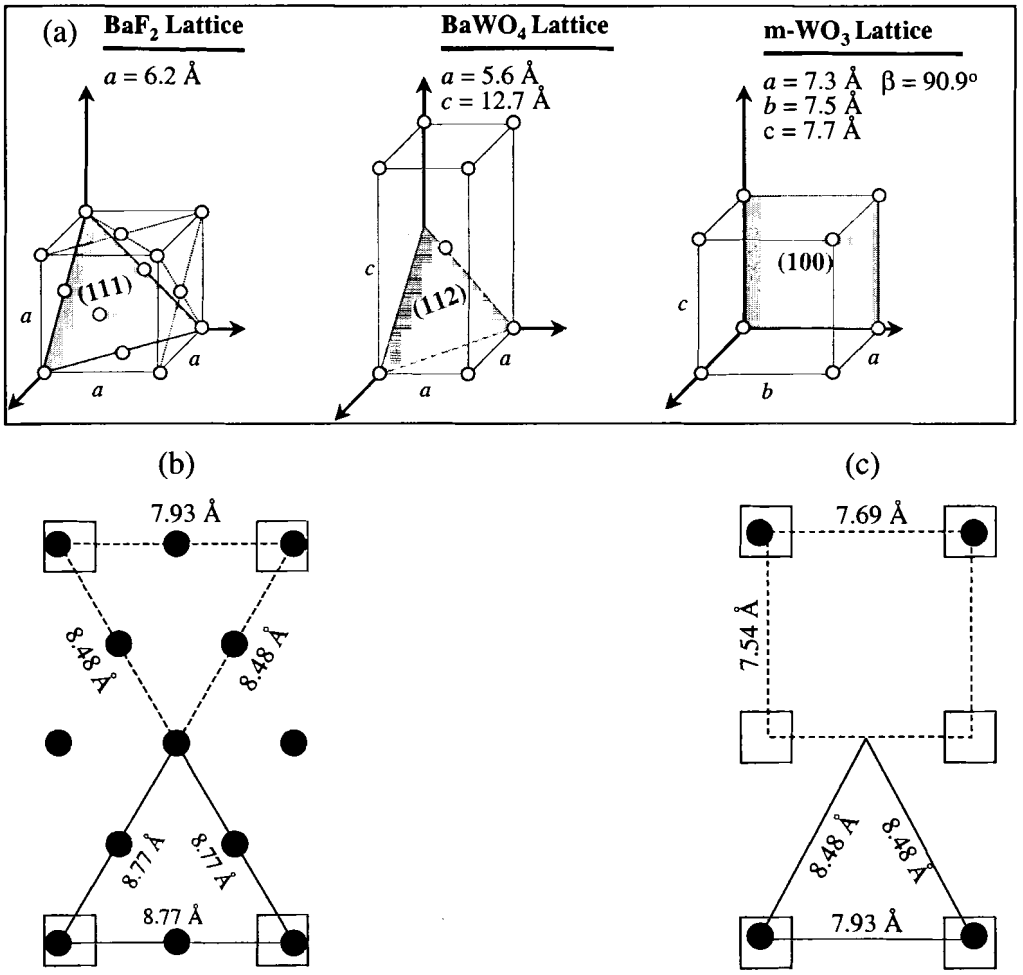


Figure 6.6 (a) Bulk lattice structures showing interfacial planes. Schematic drawings are shown for the real-space lattice matches between (b) $BaWO_4$ (112) and $BaF_2$ (111), and (c) m-$WO_3$ (100) and $BaWO_4$ (112). For both schematics, the open squares/dashed lines (solid circles/solid lines) indicate the overlayer (underlayer) mesh.

Table 6.2 - Bulk lattice misfits

| Interface | f |
|---|---|
| $BaWO_4$ (112) / $BaF_2$ (111) | 3.4%, 10.6% |
| $WO_3$ (002) / $BaWO_4$ (112) | 2.6%, 5.2% |
| $WO_3$ (020) / $BaWO_4$ (112) | 2.6%, 3.1% |
| $WO_3$ (200) / $BaWO_4$ (112) | 0.66%, 3.1% |

versus the relatively larger misfit at the $BaWO_4/BaF_2$ interface (3.4%, 10.6%), which must been compensated for by additional lattice strain and/or dislocations at this boundary. Although the misfit of 10.6% is relatively large, others have reported similar misfits in metal oxide systems for which epitaxial growth was attained.[2,3,10] Therefore, in both cases, the in-plane misfits reasonably explain the structural orientations of the $BaWO_4$ and $WO_3$ film layers. Similar misfit calculations for a possible $WO_3/BaF_2$ interface range between 14% - 20%, thereby making the existence for such a heteroepitaxial interface less likely.

### 6.5 Post-Deposition Air Annealing Experiments

The $WO_3$ grown films on $BaF_2/Si$ substrates were subjected to post-deposition air anneal studies, where XRD $\theta$-$\theta$ scans were utilized to examine the thermal stability of the $WO_3$ film microstructure, as well as to investigate the reactivity of the $WO_3 - BaF_2$ interface. Figure 6.7 displays annealing study results for two films, one initially deposited at a substrate temperature of 350°C (Figure 6.7(a)) and the other at 500°C (Figure 6.7(b)). Both films were furnace annealed in air at 400°C, followed by $\theta$-$\theta$ scans after 1 hour and 24 hour anneal times. For the 500°C substrate temperature film, the monoclinic $WO_3$ triplet and the (112) $BaWO_4$ peak maintained their intensity, suggesting that these film layers preserved their structure over the entire anneal period. The (111) $BaF_2$ peak experienced some reduction after 1 hour, suggesting structural change in the $BaF_2$ layer as a result of the 1-hour anneal. However, the $BaF_2$ peak intensity remained unchanged following a subsequent 24 hour anneal, which implied that the majority of structural changes within the $BaF_2$ layer occurred within the first hour. For the 350°C substrate

temperature film, crystallization of the (112) oriented $BaWO_4$ structure developed and the diffraction intensity increased with subsequent annealing; no formation of structured $WO_3$ developed. In addition, a peak at $2\theta = 28.0^{\circ}$ formed after 24 hours, which through pole figure measurements was identified as (004) oriented $BaWO_4$.

It is interesting to note that crystalline $BaWO_4$ formed more readily when the $WO_3$ film had a random polycrystalline as opposed to a heteroepitaxial structure. This suggests that mass transport, which occurs through a vacancy mechanism for atomic diffusion,[9] occurs more readily within the polycrystalline $WO_3$ films, presumeabley due to the greater defect density (e.g. vacancies) in these structures. In contrast, if single crystal materials are involved, then mass transport phenomena are limited to bulk lattice vacancy and/or interstitial diffusion, which are inherently slower processes due to the higher activation energies involved. Although the $BaF_2$ layer is highly crystalline, recall

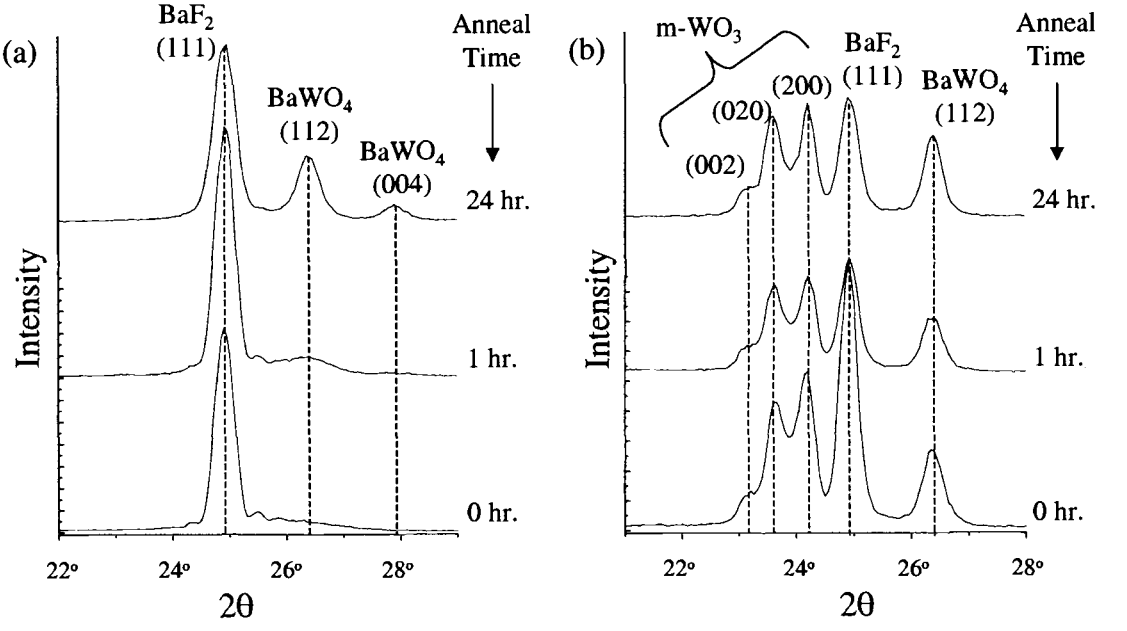


Figure 6.7 400°C post-deposition air anneal effects on $WO_3/BaWO_4/BaF_2$ microstructures for $WO_3$ films deposited at (a) 350°C and (b) 500 °C.

that well-defined grain boundaries were observed in AFM images for this surface. In general, such grain boundaries are known to serve as rapid migration paths within solids due to the low activation energies associated with diffusion processes along the boundary.[9,11-13] The presence of these migration paths in the $BaF_2$ layer would then foster inter-atomic diffusion for the larger population of mobile tungsten and oxygen atoms, as well as the smaller population of loosely bound barium and fluorine surface atoms. In all likelihood, an admixture of diffusion mechanisms are involved, where initial rapid migration down the short-circuit grain boundary network is likely slowed as tungsten and oxygen atoms leak into the $BaF_2$ lattice via lattice vacancy and/or interstitial diffusion processes to form the $BaWO_4$ structure.

### 6.6 Chapter References


[1] T. K. Chu, F. Santiago, M. Stumborg, C. A. Huber, "The role of barium in the heteroepitaxial growth of insulator and semiconductors on silicon", *Mater. Res. Soc. Symposium Proc.* 334 (1994) 501-506

[2] S. C. Moulzolf, L. J. LeGore, R. J. Lad, "Heteroepitaxial growth of tungsten oxide films on sapphire for chemical gas sensors", *Thin Solid Films* 400 (2001) 56-63.

[3] L. J. LeGore, O. D. Greenwood, J. W. Paulus, D. J. Frankel, R. J. Lad, "Controlled growth of $WO_3$ films", *J. Vac. Sci. Technol. A* 15 (1997) 1223-1227.

[4] F. P. J. Kerkhof, J. A. Moulijn, A. Heeres, *J. Electron Spectrosc. and Related Phenomenon*, 14 (1978), 453.

[5] P. G. Gassman, D. W. Macomber, S. M. Willging, *J. Amer. Chem. Soc.* 107 (1985) 2380.

[6] M. F. Stumborg, F. Santiago, T. K. Chu, K. A. Boulais, "Deposition of GaAs (111) epilayers on $BaF_2$ (111)/Si (100) heterostructures by molecular beam epitaxy", *J. Vac. Sci. Technol. A* 15 (1997) 2473-2477.

[7] JCPDS International Centre for Diffraction Data (1997).

[8] C. N. R. Rao, B. Raveau, Transition Metal Oxides, New York: VCH (1995).

[9] M. Ohring, The Materials Science of Thin Films, 2nd ed., London: Academic Press (2002).

[10] Y. J. Kim, Y. Gao, S. A. Chambers, "Selective growth and characterization of pure, epitaxial $\alpha$-$Fe_2O_3$(0001) and $Fe_2O_4$(001) films by plasma-assisted molecular beam epitaxy", *Surf. Sci.* 371 (1997) 358-370.

[11] P. G. Shewmon, Diffusion in Solids, New York: McGraw-Hill (1963).

[12] A. S. Ostrovsky, B. S. Bokstein, " Grain boundary diffusion in thin films under stress fields", *Appl. Surf. Sci.* 175 (2001) 312-318.

[13] W. Losch, P. M. Jardim, " Grain boundary diffusion and grain boundary structure in nanocrystalline thin films", *Scripta Materialia* 38 (1998) 1857-1861.

# CHAPTER 7: INTERFACIAL REACTION AND GROWTH MODEL

Up to this point, we have presented arguments that explain the symmetry and orientation aspects of the grain structures that form within the $WO_3/BaWO_4/BaF_2$ film layers both during and post film deposition. In addition, possible diffusion mechanisms have been postulated to explain the apparent migration of the tungsten and oxygen atoms, which enable the formation of the $BaWO_4$ interfacial reaction product. In this chapter, we focus on the thermodynamic aspects as well as the kinetics of the system, and consider the free energy of formation, $\Delta G$, as a driving force to produce a $BaWO_4$ compound at the $WO_3/BaF_2$ interface.

## 7.1 Free Energy of Formation Considerations

In Figures 7.1(a)-(d), an interfacial reaction and growth model depicts the different stages of film structure development that occurred during $WO_3$ deposition. In particular, during the early stages of film growth, a solid $BaF_2$ material is in the presence of a $WO_3$ flux and oxygen plasma, where the flux is assumed to be in a gaseous phase. For the initial formation of a $BaWO_4$ compound, the desired reaction equation can be described as follows:

$$BaF_2(s) + WO_3(g) + O^* \text{ (or } O^+) \rightarrow BaWO_4(s) + F_2 \qquad (7\text{-}1)$$

Table 7.1 lists the standard free energy of formation, $\Delta G^\circ$, for the corresponding products and reactants in equation (7-1). Calculating the overall $\Delta G^\circ$ for this chemical process (i.e. $\Sigma m\Delta G^\circ(\text{products}) - \Sigma n\Delta G^\circ(\text{reactants})$, $m,n$ = coefficients in chemical equation) for temperatures ranging from room temperature to 500°C results in a free energy change of

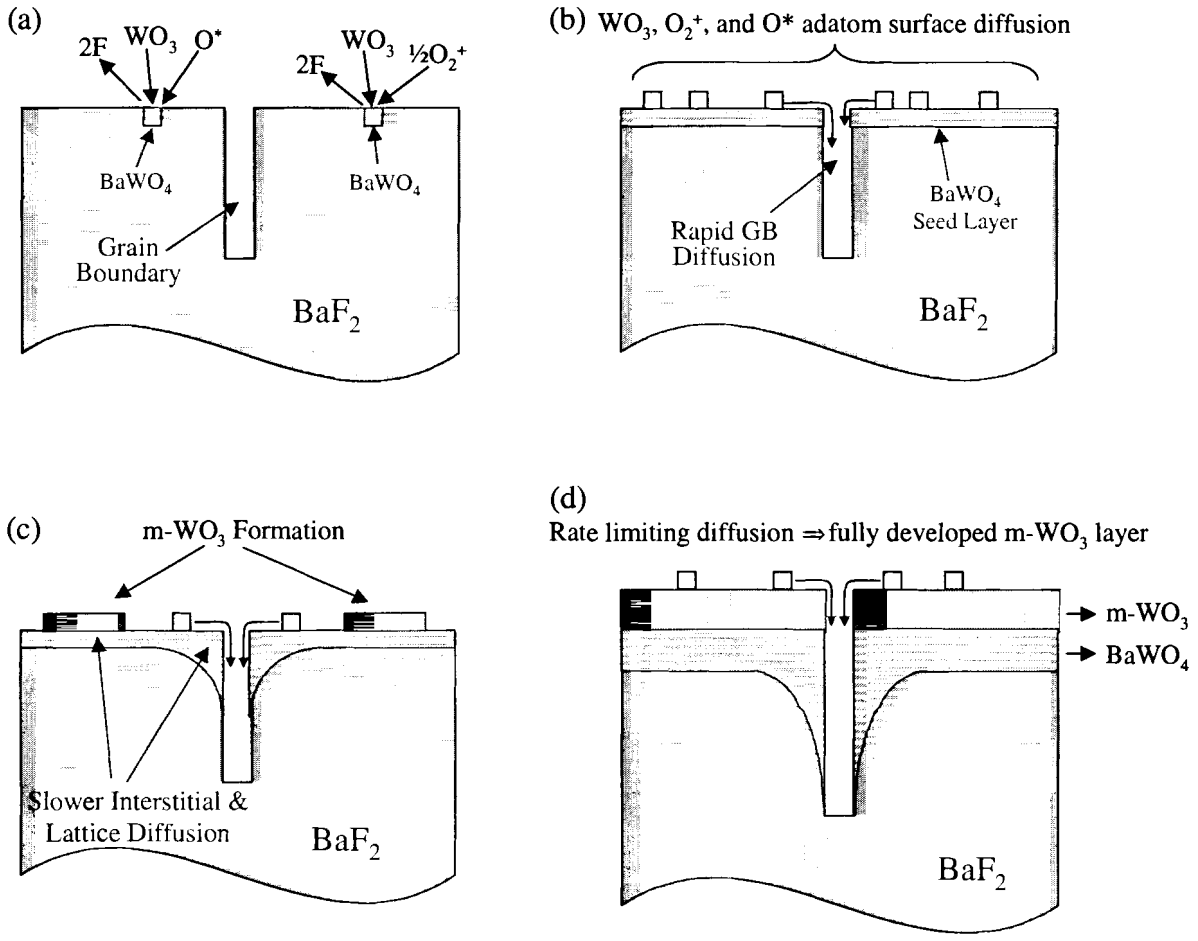


Figure 7.1(a)-(d) Interfacial reaction and growth model showing different stages of film structure development. See text for details.

Table 7.1 - Standard free energy of formation values (in kJ) (from References 1,2)

| | $\Delta G^o$ (room) | $\Delta G^o$ (500°C) |
|---|---|---|
| $BaF_2$ (s) | -1158 | -1076 |
| $WO_3$ (s) | -764 | -635 |
| $WO_3$ (g) | -277 | -249 |
| $BaWO_4$ (s) | -1598 | -1427 |
| $O^*$ (g) | 232 | 200 |
| $O^+$ (g) | 1547 | 1503 |

approximately -395 to -302 kJ/mol, respectively, when $O^*$ is considered; and –1710 to –1605 kJ/mol when $O^+$ is considered.[1,2] Therefore, given these constituent reactants, the product formation of $BaWO_4$ is highly spontaneous under standard conditions. In order to relate this quantity to the more dynamic conditions (i.e. non- standard) present during film growth, we utilize the fact that the system equilibrium constant, $K$, is related to $\Delta G^o$ by the following expression:[3,4]

$$K = e^{-\Delta G^o/RT} \tag{7-2}$$

where $R$ is the ideal gas constant and $T$ is the absolute temperature. Substituting in the $\Delta G^o$ values from above, $\log K = 68.8$ to 52.6 for $O^*$; and 111.7 to 104.8 for $O^+$ for temperatures ranging from room to 500°C.

To assign some meaning to these $K$ values, we consider that, from the laws of mass action, the equilibrium constant may alternatively be expressed in terms of the concentration levels of the reactants and products at equilibrium:[3,4]

$$K = \frac{[\text{products}]^p}{[\text{reactants}]^r} = \frac{[BaWO_4][F_2]}{[BaF_2][WO_3][O^*(\text{or } O^+)]} \tag{7-3}$$

where the brackets [ ] indicate concentration (in molarity or partial pressure), and $p$ / $r$ are the coefficients in the balanced chemical equation. In general, a system may achieve equilibrium by either moving to the right or to the left of the reaction equation. However, for instances when $K >> 1$, then the numerator in (7-3) must be much larger than the denominator. In these situations, equilibrium will then typically lie to the right, and products are favored; and conversely for $K << 1$. Therefore, knowledge of $K$ (usually expressed as $\log K$) will indicate which direction the reaction will follow in order to establish equilibrium. In regard to the calculated $K$ values above, we can therefore

conclude that the formation of a $BaWO_4$ compound is an overwhelmingly favored process.

Figure 7.1(a) illustrates the initial stage of film development, followed by the processes depicted in Figure 7.1(b), which shows the eventual seed layer formation of the $BaWO_4$ (112) structure. The formation $BaWO_4$ is a thermally driven process, such that lattice match considerations with the $BaF_2$ substrate dictates the particular orientation that the structure assumes. Indeed, the $BaWO_4$ product simply adopts the existing mesh structure offered by the (111) plane of $BaF_2$, which naturally results in the primary growth plane for a (112) orientated $BaWO_4$ tetragonal structure.

In order for the formation of $BaWO_4$ to continue, it becomes necessary for the temperature dependent diffusion of (considering all possibilities) Ba and F atoms, and/or W and O atoms to take place. Since surface and grain boundary diffusion processes require much lower activation energies than interstitial and lattice diffusion, these processes dominate during the early stages of film development. In addition, the larger population of mobile tungsten and oxygen adatoms would likely serve as the primary diffusing species for $BaWO_4$ formation as compared to barium and fluorine diffusion. Figure 7.1(b) illustrates this adatom diffusion along the surface and into the $BaF_2$ grains via the grain boundaries, thereby enabling the continued production of $BaWO_4$. The slower interstitial and lattice diffusion processes would then allow for the complete structural development of the $BaWO_4$ layer as the migrating atoms diffuse into the $BaF_2$ crystal structure.

We know that these diffusion processes during film deposition must eventually be rate limiting since monoclinic $WO_3$ eventually forms at substrate temperatures greater than

400°C, and is the only compound detected within the top layers of the film as per XPS studies. In all likelihood, the constant rate at which $WO_3$, $O_2^+$, and $O^*$ were depositing upon the surface eventually surpassed the rate at which diffusion mechanisms could facilitate $BaWO_4$ formation. This hypothesis would be consistent with grain boundary diffusion being the primary facilitator for $BaWO_4$ formation. Specifically, the initial rapid migration of adatoms would be eventually slowed by the need for interstitial and lattice diffusion processes to penetrate deeper into the $BaF_2$ lattice and continue $BaWO_4$ development. These stages of film development are illustrated in Figures 7.1(c) and (d), where it is shown how a fully developed m-$WO_3$ layer eventually forms.

## 7.2 Chapter References

[1] I. Barin, Thermochemical Data of Pure Substances, 2nd ed., New York: VCH (1993).

[2] M. W. Chase, NIST-JANAF Thermochemical Tables, New York: ACS-AIP (1998).

[3] T. L. Brown, H. E. LeMay, B. E. Bursten, Chemistry - The Central Science, Upper Saddle River: Prentice Hall (1997).

[4] R. A. Swalin, Thermodynamics of Solids, Chichester: Wiley (1972).

# CHAPTER 8: CONCLUSIONS AND FUTURE RESEARCH

We have demonstrated that a high quality (111) oriented $BaF_2$ buffer layer on single crystal Si (100) provides a good substrate for the heteroepitaxial growth of monoclinic phase $WO_3$ films. In addition, an interfacial $BaWO_4$ reaction product forms at the $WO_3$ – $BaF_2$ interface. The presence of the $BaWO_4$ phase appears to depend upon the growth temperature and diffusion processes occurring across the $WO_3/BaWO_4/BaF_2/Si$ interfaces. From XRD pole figure analyses, we identified a distinct heteroepitaxial relationship between all layers in the $WO_3$ (002), ($\bar{0}$20), (200) / $BaWO_4$ (112) / $BaF_2$ (111) / Si (100) system, such that the high symmetry of the $BaF_2$ substrate mesh induced a similar symmetry in subsequent film layers. The stability of the $WO_3$ film layer upon post-deposition air annealing provides promising results in terms of chemiresistive microsensor applications. The following section revisits these conclusions in more detail, and is followed by suggestions for preliminary sensor device application testing via 4-point van de Pauw conductivity measurements, as well as other areas of future research.

## 8.1 Conclusions

- **A high quality (111) oriented $BaF_2$ buffer layer film on a Si (100) single crystal substrate presents a suitable growth mesh for the integration of heteroepitaxial metal-oxide films with silicon.** XRD pole figure analysis revealed that the $BaF_2$ film structure was composed of four distinct cubic domains. AFM images of the film morphology suggested that these grains were approximately 500 by 500 $nm^2$ in lateral extent. Both RHEED and LEED patterns revealed how these cubic domains reduced

to two distinct hexagonal surface mesh structures, resulting in an over all 12-fold symmetric surface mesh.

- **Multi-domain heteroepitaxial monoclinic phase $WO_3$ films on $BaF_2$ (100) / Si (100) substrates have been obtained via MBE deposition methods.** XPS measurements indicated film stoichiometries that corresponded well with $WO_3$ for substrate temperatures between 400 – 500°C. Films grown below 400°C and above 500°C indicated slight reductions and excesses in the oxygen component, respectively. RHEED transmission patterns showed a superposition of multiple film structures within a single pattern for $WO_3$ films deposited between the substrate temperatures of 400 – 500°C. XRD θ-θ and pole figure measurements confirmed that these film structures corresponded to the coexistence of (002), (020), and (200) oriented monoclinic phase $WO_3$ film structures. In addition, due to the high symmetry of the substrate growth mesh, pole figures demonstrated that the $WO_3$ film maintained twelve distinct crystalline domains.
- **A thermally driven $BaWO_4$ reaction product forms at the $WO_3$ – $BaF_2$ interface.** Confirmation with XRD θ-θ and pole figure analysis indicated that a temperature dependent $BaWO_4$ reaction product formed over the same temperature ranges as the heteroepitaxial $WO_3$ film. Calculations of the free energy of formation and equilibrium constant for this system illustrate how a $BaWO_4$ reaction product is heavily favored based upon the drive toward equilibrium for the system. These reactions are likely facilitated by the presence of well-defined grain boundaries within the $BaF_2$ film layer, since these pathways would enhance atomic diffusion into the $BaF_2$ structure.

- **$WO_3$ film structures remain stable upon post-deposition air annealing.** XRD θ-θ measurements indicated that the heteroepitaxial $WO_3$ films maintained their structure upon annealing at 400°C in air for 24 hours. This result is particularly important since the potential application for these films as chemiresistive microsensing elements typically requires the sensing film to be maintained at temperatures of up to 400°C during operation.

## 8.2 Future Research

- **Conductivity measurements for selected gas exposures.** Currently at LASST, the interconnected Hall/conductivity measurement chamber is well equipped to perform fully automated conductivity measurements in a controlled gas exposure setting. Specifically, this system utilizes a 4-point van de Pauw conductivity measurement, which is comprised of four spring loaded contact probes that establish electrical contact with the sample. Although numerous attempts were made to perform these measurements on the $WO_3$ films developed in this investigation, the force of the contact pins on the film invariably caused mechanical damage during measurement that electrically shorted the probes to the Si substrate, thereby nullifying the measurements. To prevent this from occurring, one possible modification would be to incorporate a thick $SiO_2$ layer at strategic points on the Si substrate during the production of the $BaF_2$ layer. The contact probe points would then correspond to these $SiO_2$ sites after $WO_3$ coverage of the entire surface, thereby providing the necessary thickness and electrical barrier from the Si substrate.

- **Further analysis of the $BaWO_4$ reaction product layer.** Currently, we do not know how this interfacial layer would affect the response characteristics of the $WO_3$ sensing layer for typical gas exposures. Presumably, if a thick enough $BaF_2$ insulation layer remains, then conductivity changes measured within the sensing film should still be the result of gas-$WO_3$ interactions only. However, knowledge and control over the thickness of the $BaWO_4$ layer may provide additional insight as to the specific response characteristics generated by these films. Such control may be possible by varying the deposition rate during the initial stages of film growth. Specifically, slower growth rates (e.g. < 0.2 Å/s) would likely produce a thicker $BaWO_4$ layer since diffusion processes would have more time to foster this interfacial reaction. Conversely, faster rates (e.g. > 0.2 Å/s) may produce $WO_3$ growth at an earlier point during deposition due to surface kinetics. To test this hypothesis, a proposed experimental procedure would be to grow thinner films (e.g. 25 – 250 Å) within these suggested growth rate regimes. The use of thinner films would then allow for the detection of when the crossover from $BaWO_4$ to $WO_3$ occurs.
- **Synthesis and characterization of other metal-oxide systems on $BaF_2$/Si substrates.** The near single-crystal-like quality of these $BaF_2$ films, coupled with their well defined surface mesh, provides an attractive substrate material for the subsequent heteroepitaxial growth of other metal-oxide compounds. In particular, our preliminary work with titanium-oxide films deposited on these substrates has indicated the successful growth of rutile $TiO_2$ (002) oriented structures, which have exhibited similar multiplicity in grain orientations as the m-$WO_3$ films.

## BIBLIOGRAPHY


A. Agrawal, H. Habibi, "Effect of heat treatment on the structure, composition and electrochromic properties of evaporated tungsten oxide film", *Thin Solid Films* 169 (1989) 257-270.

A. Ito, K. Tsuji, T. Hosomi, T. Maki, T. Kobayashi, "Improved stability of metal-insulator-diamond semiconductor interface by employing $CaF_2$/thin $BaF_2$ composite insulator film", *Jpn. J. Appl. Phys.* 39 (2000) 4755-4756.

M.D. Antonik, J. E. Schneider, E. L. Wittman, K. Snow, J.F. Vetelino, R.J. Lad, "Microstructural effects in $WO_3$ gas-sensing films", *Thin Solid Films* 256 (1995) 247-252.

L. A. Aslanov, G.V. Fetisov, J.A.K. Howard, Crystallographic Instrumentation, New York: Oxford University Press (1998).

J. Asmussen, "A review of ECR plasma processing technology", *IEEE International Conference on Plasma Science* (1991) 139.

M. Ayyoob, M. S. Hegde, *J. Chem. Soc. Faraday Trans. I* 82 (1986) 1651.

I. Barin, Thermochemical Data of Pure Substances, 2nd ed., New York: VCH (1993).

E. P. S. Barrett, G. C. Georgiades, P. A. Sermon, "The mechanics of operation of $WO_3$-based $H_2S$ Sensors", *Sens. Actuators B* 1 (1990) 116-120.

D. Briggs, M. P. Seah, Practical Surface Analysis By Auger and X-ray Photoelectron Spectroscopy, 2nd ed., Chichester: Wiley (1990).

T. L. Brown, H. E. LeMay, B. E. Bursten, Chemistry - The Central Science, Upper Saddle River: Prentice Hall (1997).

M. W. Chase, NIST-JANAF Thermochemical Tables, New York: ACS-AIP (1998).

J. Chastain, Handbook of X-ray Photoelectron Spectroscopy, Eden Prairie: Perkin-Elmer (1992).

T. K. Chu, F. Santiago, M. Stumborg, C. A. Huber, "The role of barium in the heteroepitaxial growth of insulator and semiconductors on silicon", *Mater. Res. Soc. Symposium Proc.* 334 (1994) 501-506

B. D. Cullity, Elements of X-ray Diffraction, 2nd ed., Reading: Addison-Wesley (1978).

S. Deb, "Optical and photoelectric properties and colour centres in thin films of tungsten oxide", *Philos. Mag.* 27 (1973) 801-822.

V. E. Drozd, A. P. Baraban, I. O. Nikiforava, V. B. Aleskoviski, "Synthesis and investigation of heterooxides by ML-ALE method", *App. Surface Sci.* 12 (1997) 264-268.

A. Garg, J. A. Leake, Z. H. Barber, "Epitaxial growth of $WO_3$ films on $SrTiO_3$ and sapphire", *J. Phys. D* 33 (2000) 1048-1053.

P. G. Gassman, D. W. Macomber, S. M. Willging, *J. Am. Chem. Soc.* 107 (1985) 2380.

O. D. Greenwood, S. C. Moulzolf, P. J. Blau, R. J. Lad, "The influence of microstructure on tribological properties of $WO_3$ thin films", *Wear* 232 (1999) 84-90.

J. R. Hook, H. E. Hall, Solid State Physics, 2nd ed., Chichester: Wiley (1991).

JCPDS International Centre for Diffraction Data (1997).

F. Jona, J. A. Strozier Jr., W. S. Yang, "Low-energy electron diffraction for surface structure analysis", *Rep. Prog. Phys.* 45 (1982) 527-585.

F. P. J. Kerkhof, J. A. Moulijn, A. Heeres, *J. Electron Spectrosc. and Related Phenomenon* 14 (1978), 453.

Y. J. Kim, Y. Gao, S. A. Chambers, "Selective growth and characterization of pure, epitaxial $\alpha$-$Fe_2O_3$(0001) and $Fe_2O_4$(001) films by plasma-assisted molecular beam epitaxy", *Surf. Sci.* 371 (1997) 358-370.

Y. Kobayashi, S. Terada, K. Kubota, "Epitaxial growth of $WO_3$ thin films on MgO and $Al_2O_3$", *Thin Solid Films* 168 (1989) 133-139.

J. P. LaFemina, "Theory of insulator surface structures", Handbook of Surface Science, Vol. 1, Ed. W. N. Unertl, New York: Elsevier (1996) 137-184.

E. Lassner, W. Schubert, Tungsten: Properties, Chemistry, Technology of the Element, Alloys, and Chemical Compounds, New York: Kluwer Academic / Plenum Publishers (1999).

L. J. LeGore, O. D. Greenwood, J. W. Paulus, D. J. Frankel, R. J. Lad, "Controlled growth of $WO_3$ films", *J. Vac. Sci. Technol. A* 15 (1997) 1223-1227.

L. J. LeGore, K. Snow, J. D. Galipeau, J. F. Vetelino, "The optimization of a tungsten trioxide film for application in a surface acoustic wave gas sensor", *Sens. Actuators B* 35-36 (1996) 164-169.

W. Losch, P. M. Jardim, " Grain boundary diffusion and grain boundary structure in nanocrystalline thin films", *Scripta Materialia* 38 (1998) 1857-1861.

H. C. Lu, H. R. Fetterman, C. J. Chen, C. Hsu, T. M. Chen, "Growth and characterization of MBE-grown thin films of InSb on Si", *Solid-State Electron.* 36 (1993) 533-538.

K. Mae, V. Moshchalkov, Y. Bruynseraede, "Intensity profiles along the RHEED streaks for various thin film surface morphologies", *Thin Solid Films* 340 (1999) 145-152.

K. Marszalek, "Magnetron-sputtered $WO_3$ films for electrochromic devices", *Thin Solid Films* 175 (1989) 227-233.

K Miyake, H. Kaneko, M. Sano, N. Suedomi, "Physical and electrochromic properties of the amorphous and crystalline tungsten oxide thick films prepared under reducing atmosphere", *J. Appl. Phys.* 55 (1984) 2747-2753.

S. C. Moulzolf, L .J. LeGore, R. J. Lad, "Heteroepitaxial growth of tungsten oxide films on sapphire for chemical gas sensors", *Thin Solid Films* 400 (2001) 56-63.

MPDR 610I ECR Microwave Plasma Source product brochure, Wavemat, Inc. Plymouth, MI.

S. F. Murray, S. J. Calabrese, "Effects of solid lubricants on low speed sliding behavior of silicon nitride at temperatures to 800°C", *Lubr. Eng.* 49 (1993) 387.

M. Ohring, The Materials Science of Thin Films, 2nd ed., London: Academic Press (2002).

M. A. Omar, Elementary Solid Sate Physics: Principles and Applications, Reading: Addison-Wesley (1975).

A. S. Ostrovsky, B. S. Bokstein, " Grain boundary diffusion in thin films under stress fields", *Appl. Surf. Sci.* 175 (2001) 312-318.

M. Penza, C. Martucci, G. Cassano, "$NO_x$ gas sensing characteristics of $WO_3$ thin films activated by noble metals (Pd, Pt, Au) layers", *Sens. Actuators B* 50 (1998) 52-59.

M. Penza, L Vasanelli, "SAW $NO_x$ gas sensor using $WO_3$ thin-film sensitive coating", *Sens. Actuators B* 41 (1997) 31-36.

C. N. R. Rao, B. Raveau, Transition Metal Oxides, New York: VCH Publishers (1995).

F. Santiago, D. Wood, T. K. Chu, C. A. Huber, "Interface characterization of PbTe/BaSi/Si heterostructures grown using MBE", *Mater. Res. Soc. Symposium Proc.* 281 (1993) 603-608.

L. G. Schulz, "A direct method of determining preferred orientation of a flat reflection sample using a geiger counter X-ray spectrometer", *J. Appl. Phys.* 20 (1949) 1030-1033.

H. Seyama, M. Soma, *J. Chem. Soc. Faraday Trans. I* 80 (1984) 237.

P. G. Shewmon, Diffusion in Solids, New York: McGraw-Hill (1963).

D. J. Smith, J. F. Vetelino, R. S. Falconer, E. L. Wittman, "Stability, sensitivity, and selectivity of tungsten trioxide films for sensing applications", *Sens. Actuators B* 13-14 (1993) 264-268.

M. F. Stumborg, F. Santiago, T. K. Chu, K. A. Boulais, "Deposition of GaAs (111) epilayers on $BaF_2$ (111)/Si (100) heterostructures by molecular beam epitaxy", *J. Vac. Sci Technol. A* 15 (1997) 2473-2477.

H.T. Sun, C. Cantalini, L. Lozzi, M. Passacantando, S. Santucci, M. Pelino, "Microstructural effect on $NO_2$ sensitivity of $WO_3$ thin film gas sensors Part 1. Thin film devices, sensors and actuators", *Thin Solid Films* 287 (1996) 258-263.

R. A. Swalin, Thermodynamics of Solids, Chichester: Wiley (1972).

Z. L. Wang, Reflection Electron Microscopy and Spectroscopy for Surface Analysis, Cambridge: Cambridge University Press (1996).

D. B. Williams, C. B. Carter, Transmission Electron Microscopy, New York: Plenum Press (1996).

R. W. G. Wyckoff, Crystal Structures, Vol. 1, New York: Wiley (1964).

M. Yoshimoto et al., "Room-temperature epitaxial growth of $CeO_2$ thin films on Si(111) substrates for fabrication of sharp oxide/silicon interface", *Jpn. J. Appl. Phys. Part 2: Letters* 34 (1995) L688-L690.

## BIOGRAPHY OF THE AUTHOR

Luke D. Doucette was born in Van Buren, Maine on January 6, 1970. He was raised in Van Buren, and graduated from Van Buren District Secondary School in 1988. He attended the University of Southern Maine in Portland, Maine and graduated with honors in 1992 with a BS in Business Administration. He subsequently moved to Boston, Massachusetts where he held a supervisory role while working for an insurance company. In 1997, he attended the University of Maine in Orono, Maine and graduated with honors in 2000 with a BS in Physics. During this period, he worked as a laboratory assistant at the Laboratory for Surface Science and Technology (LASST) located on the University of Maine campus, where he gained valuable experiences in the fields of materials science and applied physics. In the summer of 2000, he entered the graduate program for Physics at the University of Maine, and anticipates completing his Master's degree in Physics with a research concentration in novel semiconducting material applications.

Luke was married in August of 1994 to wife, Christine, and has two lovely daughters, Olivia, born in August of 1998, and Gabrielle, born in October of 2001. Luke is a candidate for the Master of Science degree in Physics from The University of Maine in December, 2002.